Inorganic Chemistry

pubs.acs.org/IC

Article

Panchromatic Absorption and Oxidation of an Iron(II) Spin Crossover Complex

Johannes Moll, Christoph Förster, Alexandra König, Luca M. Carrella, Manfred Wagner, Martin Panthöfer, Angela Möller, Eva Rentschler, and Katja Heinze*

Cite This: *Inorg. Chem.* 2022, 61, 1659−1671

Read Online

ACCESS | Metrics & More | Article Recommendations | Supporting Information

ABSTRACT: In order to expand and exploit the useful properties of d^6-iron(II) and d^5-iron(III) complexes in potential magnetic, photophysical, or magnetooptical applications, crucial ligand-controlled parameters are the ligand field strength in a given coordination mode and the availability of suitable metal and ligand frontier orbitals for charge-transfer processes. The push−pull ligand 2,6-diguanidylpyridine (dgpy) features low-energy π^* orbitals at the pyridine site and strongly electron-donating guanidinyl donors combined with the ability to form six-membered chelate rings for optimal metal−ligand orbital overlap. The electronic ground states of the pseudo-octahedral d^6- and d^5-complexes ***mer*-[Fe(dgpy)$_2$]$^{2+}$**, ***cis-fac*-[Fe(dgpy)$_2$]$^{2+}$**, and ***mer*-[Fe(dgpy)$_2$]$^{3+}$** as well as their charge-transfer (CT) and metal-centered (MC) excited states are probed by variable temperature UV/vis absorption, NMR, EPR, and Mössbauer spectroscopy, magnetic susceptibility measurements at variable temperature as well as quantum chemical calculations.

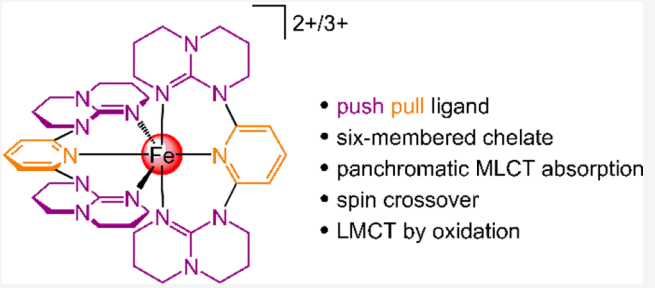

INTRODUCTION

The coordination chemistry of pseudo-octahedral iron(II) and iron(III) complexes is dominated by variable spin states that can be realized and the resulting well-explored spin-crossover (SCO) phenomenon.[1−4] Temperature, pressure, and light stimuli can switch between the low- and high-spin states of iron(II) complexes which possess a suitable ligand field strength (d^6-iron(II): $^1A_{1g}$, $^5T_{2g}$ in O_h symmetry).[1−3,5,6] The optical switching process has been termed light-induced excited spin state trapping (LIESST). Excitation of the prototypical complex [Fe(ptz)$_6$]$^{2+}$ (ptz = 1-propyl tetrazole) in its low-spin state ($^1A_{1g}$) with green light at low temperature populates the ligand field (or metal-centered) states ($^1T_{1g}$ and $^1T_{2g}$). Fast and efficient double intersystem crossing (ISC) via the ligand field triplet states ($^3T_{1g}$/$^3T_{2g}$) either leads to relaxation back to the low-spin state or to population of the metastable high-spin state.[7,8] Prolonged irradiation at sufficiently low temperature can fully populate the metastable high-spin state. Iron(II) complexes with suitable chromophoric ligands can be initially excited into singlet metal-to-ligand charge-transfer (^{1}MLCT) states and subsequently undergo ISC processes to the metastable high-spin ligand field state.[9−11] Selective excitation of the low-temperature trapped metastable high-spin state of [Fe(ptz)$_6$]$^{2+}$ with 820 nm light repopulates the low-spin ground state (reverse-LIESST effect). The lifetime of the metastable high-spin state depends on the conditions, especially the available thermal energy. At room temperature, relaxation of photoexcited iron(II) complexes with nearly octahedral [FeN$_6$] coordination, e.g., [Fe(dcpp)$_2$]$^{2+}$ and [Fe(dcpp)(ddpd)]$^{2+}$ (Chart 1), to the low-spin ground state occurs on the pico- to nanosecond time scale (dcpp = 2,6-bis(2-carboxypyridyl)pyridine; ddpd = *N*,*N*′-dimethyl-*N*,*N*′-dipyridin-2-ylpyridine-2,6-diamine).[10−12]

Beyond the thermal and light-switchable SCO, attempts to install low-energy ^{3}MLCT states as lowest excited states in iron(II) complexes have become a vivid, yet challenging research focus.[13] This is inspired by the useful photophysics of homologous ruthenium(II) complexes, especially with a [RuN$_6$] coordination sphere, such as [Ru(bpy)$_3$]$^{2+}$ derivatives and analogues (bpy = 2,2′-bipyridine). The aim is to increase the lifetime of the ^{3}MLCT state of iron(II) complexes by hindering the fast relaxation to the high-spin state to allow for ^{3}MLCT phosphorescence and bimolecular reactivity of the ^{3}MLCT excited state (photoredox catalysis).[13−15] Current attempts focus on increasing the intrinsically weak ligand field splitting of iron(II) by using strong field ligands such as carbene donors and by improving metal−ligand orbital overlap (high-energy ^{3}T and ^{5}T states) and on decreasing the $^{1/3}$MLCT energies by push−pull effects, e.g., in [Fe(dcpp)-

Received: November 9, 2021
Published: January 12, 2022

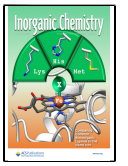

https://doi.org/10.1021/acs.inorgchem.1c03511
Inorg. Chem. 2022, 61, 1659−1671

Chart 1. Pseudo-Octahedral Transition Metal Complexes with Six-Membered Chelate Rings Relevant to This Study

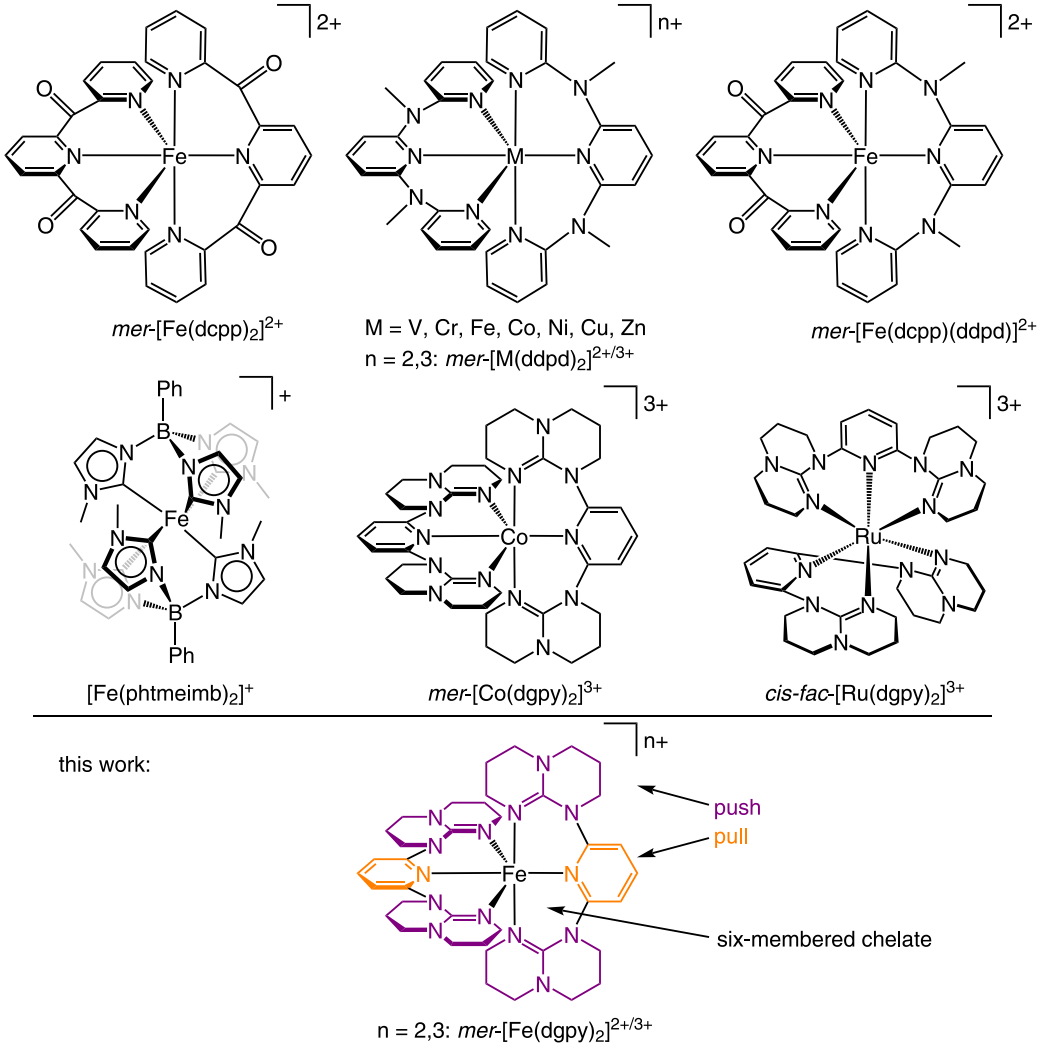

(ddpd)]$^{2+}$ (Chart 1).[12,16] The latter strategy additionally improves the absorption across the visible and near-infrared spectral region (panchromatic absorption) which is desirable to harvest a higher portion of the sunlight.[17,14] The highest reported ^{3}MLCT lifetimes of iron(II) complexes and bimolecular reactivity were achieved using carbene, cyclometalating, or (phenanthridin-4-yl)(quinolin-8-yl)amido ligands.[18−26] Iron(II) complexes of *N*-heterocyclic carbene ligands with appended anthracenyl or pyrenyl chromophores display ligand-based fluorescence with nanosecond lifetimes,[27] while appended zinc porphyrins enable a weak emission with ^{3}MLCT character and a ^{3}MLCT lifetime of 160 ps.[28]

Oxidation of iron(II) complexes to their d^5-iron(III) congeners in a strong field environment can yield luminescent complexes yet with an inverted charge-transfer direction (LMCT). The low-spin iron(III) complexes $[Fe(btz)_3]^{3+}$ and $[Fe(phtmeimb)_2]^{+}$ (btz = 3,3′-dimethyl-1,1′-bis(*p*-tolyl)-4,4′-bis(1,2,3-triazol-5-ylidene); phtmeimb$^-$ = [phenyl(tris(3-methylimidazolin-2-ylidene))borate(1−), Chart 1) are luminescent at room temperature with ^{2}LMCT fluorescence lifetimes of 100 ps and 2 ns, respectively.[29,30] The d^6-low-spin cobalt(III) complex *mer*-$[Co(dgpy)_2]^{3+}$ (dgpy = 2,6-diguanidylpyridine, Chart 1) with a tridentate pyridine/guanidine ligand possesses an emissive ^{3}LMCT state with a 5.07 ns lifetime.[31] On the other hand, luminescence properties of the low-spin d^5-complex *cis-fac*-$[Ru(dgpy)_2]^{3+}$ were not reported (Chart 1).[32] Possibly the more flexible facial coordination prevents efficient luminescence. Similar to dgpy, *cis-fac* isomers of ddpd complexes have been reported occasionally as well, yet the thermodynamically preferred coordination mode for ddpd is meridional (Chart 1).[33,34] The exceptionally successful complexes with LMCT luminescence, $[Fe(phtmeimb)_2]^{+}$ and $[Co(dgpy)_2]^{3+}$, possess six-membered chelate rings with the metal center. This geometrical feature is also shared by most successful spin-flip emitters based on chromium(III) and vanadium(III) using, for example, the ddpd ligand (Chart 1; $[M(ddpd)_2]^{3+}$, M = Cr, V).[34−37]

This study probes the dgpy ligand possessing electron donating guanidine and electron accepting pyridine units (push−pull) at the same time and forming six-membered chelate rings in d^6-iron(II) and d^5-iron(III) complexes (Chart 1 bottom) to install low-energy charge-transfer and high-energy metal-centered states for potential magnetic and optical applications. In addition, the effect of the geometric flexibility of dgpy on excited state levels will be addressed.

EXPERIMENTAL SECTION

General Procedures. All reagents were used as-received from commercial suppliers (Acros Organics, Alfa Aesar, Fischer, and Sigma-

https://doi.org/10.1021/acs.inorgchem.1c03511
Inorg. Chem. 2022, 61, 1659−1671

Aldrich). CH_3CN and CD_3CN were distilled from CaH_2. Diethyl ether and THF were distilled from sodium and potassium, respectively. d_6-Acetone was degassed by purging with argon and dried over molecular sieve 4 Å. The ligand dgpy was synthesized according to a literature procedure.[32] ^1H NMR spectra were recorded on a Bruker Avance DRX 400 spectrometer (400.31 MHz), on a Bruker Avance III HD 400 spectrometer (400.13 MHz), or on a Bruker Avance III 600 spectrometer (600.13 MHz) with a 5 mm TCI-CryoProbe with a z-gradient and ATM. Temperature-dependent ^1H NMR spectra were recorded on a Bruker Avance III HD 500 spectrometer (500.15 MHz) with a BBFO 5 mm $^1H/X/^{19}F$ probe head (z-gradient, sweep width of 250 ppm, 90° pulse angle for 14.7 μs) using a dewar-N_2 cooling unit. A methanol standard was used for temperature calibration. All resonances are reported in ppm versus the solvent signal as an internal standard (CD_3CN, δ = 1.940; d_6-acetone, δ = 2.050 ppm).[38] ESI mass spectra were recorded on an Agilent 6545 QTOF-MS spectrometer. ATR IR spectra were recorded with a Bruker ALPHA II FT-IR spectrometer with a Platinum Di-ATR module inside an argon filled glovebox. Elemental analyses were performed by the Microanalytical Laboratory of the Department of Chemistry of the University of Mainz using an Elementar vario EL Cube. X-band EPR spectra were recorded on a Miniscope MS 300 (Magnettech GmbH, Germany) with a frequency counter FC 400 (Magnettech GmbH, Germany) at a microwave frequency of 9.39 GHz in frozen butyronitrile (77 K). Mn^{2+} in ZnS was used as the external standard (g = 2.118, 2.066, 2.027, 1.986, 1.946, 1.906). Simulations were performed with the program package Easyspin for MatLab (R2016b).[39] Electrochemical experiments were carried out on a BioLogic SP-200 voltammetric analyzer using platinum wires as counter and working electrodes and 0.01 M $Ag/AgNO_3$ as the reference electrode. The measurements were carried out at a scan rate of 100 mV s^{-1} for cyclic voltammetry experiments and at 50 mV s^{-1} for square-wave voltammetry experiments using 0.1 M $[^nBu_4N][PF_6]$ as the supporting electrolyte in CH_3CN. Potentials are referenced to the ferrocene/ferrocenium couple ($E_{1/2}$ = 110 ± 5 mV under the experimental conditions). UV/vis spectroelectrochemical experiments were performed using a BioLogic SP-50 voltammetric analyzer and a Specac omni-cell liquid transmission cell with CaF_2 windows equipped with a Pt-gauze working electrode, a Pt-gauze counter electrode, and a Ag wire as pseudoreference electrode, melt-sealed in a 2 mM polyethylene spacer (approximate path length 1 mm) in CH_3CN containing 0.1 M $[^nBu_4N][PF_6]$.[40] UV/vis spectra were recorded on a Varian Cary 5000 spectrometer using 1.0 cm cells with a Schott valve. Emission spectra were recorded on a Varian Cary Eclipse spectrometer. For temperature-dependent optical spectroscopy, a freshly prepared butyronitrile[41] solution of the complex was filled into a quartz cuvette in an argon filled glovebox, and the cuvette was sealed and transferred to an Oxford cryostat (Oxford instruments OptistatDN) or Varian Cary Peltier element, respectively. DC magnetic studies were performed with a Quantum Design MPMS-XL-7 SQUID magnetometer on a powdered microcrystalline sample. Variable temperature susceptibility data were collected in a temperature range of 150−350 K under an applied field of 0.1 T. Experimental susceptibility data were corrected for the underlying diamagnetism using Pascal's constants. The temperature-dependent magnetic contribution of the holder was experimentally determined and subtracted from the measured susceptibility data. ^{57}Fe Mössbauer spectra were collected using a custom-built setup adapted with a Montana C2 closed-cycle cryostat at temperatures of 100, 200, 250, 275, and 300 K using an approximately 180 mg sample in a 2 cm^2 PE vessel. Original spectra were folded according to a calibration with α-Fe (ambient conditions). Spectra were fitted using the Voigt-based-fitting (VBF) approach[42] as implemented in the software package Recoil.[43]

Intensity data for crystal structure determination were collected with a STOE IPDS-2T diffractometer from STOE & CIE GmbH for the PF_6^- salts and with a STADIVARI diffractometer from STOE & CIE GmbH for the OTf^- salt, respectively, using Mo−K_α radiation (λ = 0.71073 Å). The diffraction frames were integrated using the STOE X-Area software package[44] and corrected for absorption with MULABS[45] of the PLATON software package[46] for the PF_6^- salts and with STOE LANA[47] for the OTf^- salt, respectively.

The structures were solved and refined by the full-matrix method based on F^2 using the SHELXL 2018/3 software package[48,49] for the PF_6^- salts and using the SHELXL 2016/6 software package[48,50] for the OTf^- salt, respectively, and the ShelXle graphical interface.[51] All non-hydrogen atoms were refined anisotropically, while the positions of all hydrogen atoms were generated with appropriate geometric constraints and allowed to ride on their respective parent atoms with fixed isotropic thermal parameters. Crystallographic data for the structures reported in this paper have been deposited with the Cambridge Crystallographic Data Centre as supplementary publication no. CCDC-2062797, CCDC-2062796, and CCDC-2059034 for $\mathbf{1}[\mathbf{OTf}]_2\times0.5CH_3CN$, $\mathbf{1}[\mathbf{PF_6}]_2\times CH_3CN$, and $\mathbf{1}[\mathbf{PF_6}]_3\times1.5CH_3CN$, respectively.

Crystallographic Data of $\mathbf{1[OTf]_2\times CH_3CN}$. $C_{40}H_{54}F_6FeN_{14}O_6S_2\times0.5CH_3CN$ (1081.47); orthorhombic; $Pna2_1$; a = 23.8225(6) Å, b = 14.0082(3) Å, c = 14.0621(4) Å; V = 4692.7(2) $Å^3$; Z = 4; density, calcd. = 1.531 g cm^{-3}, T = 173(2) K, μ = 0.499 mm^{-1}; $F(000)$ = 2252.0; crystal size 0.480 × 0.223 × 0.080 mm; θ = 2.052 to 25.995 deg.; $-29 \le h \le 28$, $-17 \le k \le 17$, $-17 \le l \le 17$; rfln collected = 56186; rfln unique = 9195 [R(int) = 0.0609]; completeness to θ = 25.995 deg. = 100.0%; semiempirical absorption correction from equivalents; max. and min. transmission 0.9816 and 0.1681; data 9195; restraints 188; parameters 779; goodness-of-fit on F^2 = 1.034; final indices [$I > 2\sigma(I)$] R_1 = 0.0658, wR_2 = 0.1718; R indices (all data) R_1 = 0.0806, wR_2 = 0.1867; largest diff. peak and hole 0.662 and −0.528 e $Å^{-3}$, absolute structure parameter = −0.01(2).

Crystallographic Data of $\mathbf{1[PF_6]_2\times CH_3CN}$. $C_{38}H_{54}F_{12}FeN_{14}P_2\times CH_3CN$ (1093.79); orthorhombic; $Pna2_1$; a = 23.548(5) Å, b = 13.868(3) Å, c = 13.904(3) Å; V = 4540.5(16) $Å^3$; Z = 4; density, calcd. = 1.600 g cm^{-3}, T = 120(2) K, μ = 0.504 mm^{-1}; $F(000)$ = 2264.0; crystal size 0.730 × 0.500 × 0.300 mm; θ = 2.701 to 27.938 deg.; $-31 \le h \le 30$, $-15 \le k \le 18$, $-18 \le l \le 18$; rfln collected = 38787; rfln unique = 10803 [R(int) = 0.0339]; completeness to θ = 25.242 deg. = 99.9%; semiempirical absorption correction from equivalents; max. and min. transmission 1.12683 and 0.91783; data 10803; restraints 13, parameters 670; goodness-of-fit on F^2 = 1.053; final indices [$I > 2\sigma(I)$] R_1 = 0.0293, wR_2 = 0.0724; R indices (all data) R_1 = 0.0311, wR_2 = 0.0737; largest diff. peak and hole 0.402 and −0.233 e $Å^{-3}$, absolute structure parameter = −0.006(2).

Crystallographic Data of $\mathbf{1[PF_6]_3\times 1.5CH_3CN}$. $C_{38}H_{54}F_{18}FeN_{14}P_3\times1.5CH_3CN$ (1259.29); monoclinic; Ia; a = 16.368(3) Å, b = 36.078(7) Å, c = 17.311(4) Å, β = 92.05°; V = 10216(4) $Å^3$; Z = 8; density, calcd. = 1.638 g cm^{-3}, T = 120(2) K, μ = 0.506 mm^{-1}; $F(000)$ = 5168.0; crystal size 0.240 × 0.147 × 0.040 mm; θ = 2.611 to 26.000 deg.; $-20 \le h \le 20$, $-44 \le k \le 44$, $-21 \le l \le 20$; rfln collected = 32744; rfln unique = 18600 [R(int) = 0.0905]; completeness to θ = 25.242 deg. = 99.9%; semiempirical absorption correction from equivalents; max. and min. transmission 1.16201 and 0.84225; data 18600; restraints 1139, parameters 1609; goodness-of-fit on F^2 = 1.128; final indices [$I > 2\sigma(I)$] R_1 = 0.0805, wR_2 = 0.1536; R indices (all data) R_1 = 0.1335, wR_2 = 0.1864; largest diff. peak and hole 0.577 and −0.603 e $Å^{-3}$, absolute structure parameter = −0.01(2).

Density Functional Theory (DFT) calculations were carried out using the ORCA program package (version 4.1.1).[52] All calculations were performed using the B3LYP functional[53−55] employing the RIJCOSX approximation.[56,57] Relativistic effects were calculated at the zeroth order regular approximation (ZORA) level.[58] The ZORA keyword automatically invokes relativistically adjusted basis sets. To account for solvent effects, a conductor-like screening model (CPCM) modeling acetonitrile was used in all calculations.[59,60] Geometry optimizations were performed using Ahlrichs' polarized valence triple-ζ basis set (def2-TZVP).[61,62] Atom-pairwise dispersion correction was performed with the Becke-Johnson damping scheme (D3BJ).[63,64] The energy of the electronic states and presence of energy minima were checked by numerical frequency calculations.

https://doi.org/10.1021/acs.inorgchem.1c03511
Inorg. Chem. 2022, 61, 1659−1671

Explicit counterions and/or solvent molecules were not taken into account. The charge-transfer number analyses of the time-dependent DFT (TDDFT) calculated transitions were done using TheoDORE 2.2.[65,66]

Synthesis of ***1[OTf]$_2$***. A solution of 108 mg (0.306 mmol, 2.2 equiv) of dgpy in dry THF (13 mL) was added to a suspension of 70 mg (0.14 mmol, 1.0 equiv) of Fe[OTf]$_2$ in dry THF (50 mL). The solution turned red. Dark red crystals precipitated after stirring at ambient temperature for 24 h. The product was collected by filtration under inert conditions and purified by crystallization via slow diffusion of dry diethyl ether into a concentrated solution in acetonitrile to yield 65 mg (0.06 mmol, 44%) of **1[OTf]$_2$**. Elem. anal. calcd. for $C_{40}H_{54}F_6FeN_{14}O_6S_2$: C, 45.29; H, 5.13; N, 18.48. Found: C, 45.26; H, 5.33; N, 18.88. ^{1}H NMR (400 MHz, CD_3CN, 293 K): δ/ppm = 29.3 (s, 4 H), 14.8 (s, 8 H), 12.6 (s, 4 H), 11.6 (s, 3.63 H), 9.3 (s, 4 H), 8.0 (s, 2 H), 6.9 (s, 4 H), 4.8 (s, 4 H), −0.1 (s, 4 H), −4.4 (s, 4.69 H). ^{1}H NMR (400 MHz, d_6-acetone, 293 K): δ/ppm = 31.8 (s, 4 H), 16.2 (s, 4 H), 16.0 (4 H), 14.0 (s, 4 H), 12.1 (s, 2.30 H), 10.2 (s, 4 H), 8.3 (s, 2 H), 7.5 (s, 4 H), 5.0 (s, 4 H), 0.1 (s, 4 H), −4.5 (s, 4 H). ^{1}H NMR (500 MHz, d_6-acetone, 193 K; ***mer*-1^{2+}**): δ/ppm = 8.71 (s, 3 H), 8.16 (s, 2 H), 4.37 (m, 8 H), 3.85 (s, 4 H), 3.73 (m, 12 H), 2.42 (m, 8 H), 1.78 (s, 4 H). ^{1}H NMR (500 MHz, d_6-acetone, 193 K; ***cis-fac*-1^{2+}**): δ/ppm = 98.6 (s), 96.2 (s), 65.9 (s), 61.6 (s), 55.2 (s), 37.9 (s), 34.2 (s), 33.3 (s), 30.2 (s), 22.7 (s), 17.2 (s), 11.4 (s), −9.9 (s), −14.3 (s), −15.0 (s), −26.2 (s), −37.8 (s), −48.3 (s), −66.1 (s). For both isomers, some integrals of ^{1}H resonances are lower than expected for dgpy ligands. Furthermore, traces of uncoordinated ligand (detected in the 600 MHz ^{1}H NMR spectrum), presumably formed by dissociation from the complex, show integrals lower than expected for the aliphatic protons of dgpy. We suspect that the dgpy ligand coordinated to iron(II) undergoes partial H/D exchange at these positions with the deuterated solvent, which reduces the integrals for these proton resonances. MS (ESI$^+$): m/z (%) = 354.240 (100, [dgpy+H]$^+$), 381.199 (19, [Fe(dgpy)$_2$]$^{2+}$), 504.199 (33, {[dgpy+2H][OTf]}$^+$), 911.351 (20, {[Fe(dgpy)$_2$][OTf]}$^+$). MS (HR-ESI$^+$): calcd. for $C_{39}H_{54}F_3FeN_{14}O_3S^+$: m/z = 911.3520. Found: 911.3510. IR (ATR): $\tilde{\nu}$/cm^{-1} = 3104 (vw), 2944 (vw), 2861 (vw), 1606 (m), 1590 (m), 1502 (w), 1453 (w, sh), 1430 (m), 1374 (w), 1325 (w), 1301 (vw), 1263 (s), 1219 (w), 1198 (m), 1140 (s), 1110 (w, sh), 1062 (vw), 1028 (s), 994 (vw, sh), 911 (vw), 885 (vw, sh), 850 (vw), 806 (w), 752 (vw), 731 (vw), 706 (vw, sh), 634 (vs), 610 (vw, sh), 571 (w), 557 (w), 516 (m). UV/vis (CH_3CN, 295 K): λ_{max}/nm (ε/M^{-1} cm^{-1}) = 222 (41900), 255 (26700), 302 (15200), 466 (961), 530 (996), 582 nm (957). CV (CH_3CN, 0.1 M [^{n}Bu$_4$N][PF$_6$] vs ferrocene, 295 K): $E_{1/2}$/V = −0.65 (rev., ***mer*-1$^{2+/3+}$**), −0.37 (rev., ***cis-fac*-1$^{2+/3+}$**), +0.97 V (qrev., coordinated dgpy$^{0/+}$).

Synthesis of ***1[PF$_6$]$_2$***. **1[OTf]$_2$** (16 mg, 0.015 mmol, 1.0 equiv) and [^{n}Bu$_4$N][PF$_6$] (310 mg, 0.800 mmol, 53 equiv) were dissolved in dry acetonitrile (2 mL). Slow diffusion of diethyl ether into this solution yielded crystals suitable for XRD analysis.

Synthesis of ***1[PF$_6$]$_3$***. **1[OTf]$_2$** (34 mg, 0.032 mmol, 1.0 equiv) and [FeCp$_2$][PF$_6$] (11 mg, 0.032 mmol, 1.0 equiv) were dissolved in dry solvent (2 mL). CD_3CN, butyronitrile, and CH_3CN were used for in situ ^{1}H NMR, EPR, and optical spectroscopy, respectively. Slow diffusion of diethyl ether into a CH_3CN solution of **1[OTf]$_2$** (55.7 mg, 0.0525 mmol, 1.0 equiv), [FeCp$_2$][PF$_6$] (17.4 mg, 0.0526 mmol, 1.0 equiv), and [^{n}Bu$_4$N][PF$_6$] (1058 mg, 2.731 mmol, 52 equiv) yielded red crystals (23.4 mg, 0.0195 mmol, 41%). Elem. anal. calcd. for $C_{38}H_{54}F_{18}FeN_{14}P_3 \times 1.3\ CH_3CN$: C, 38.98; H, 4.67; N, 17.13, found: C, 38.48; H, 4.87; N, 17.64. ^{1}H NMR (400 MHz, CD_3CN, 293 K): δ/ppm = 54.1 (s, 4 H), 31.1 (s, 4 H), 25.9 (s, 4 H), 24.6 (s, 4 H), 20.8 (s, 4 H), 9.2 (s, 2 H), 7.8 (s, 4 H), 5.2 (s, 4 H), 3.3 (s, 4H), 0.1 (s, 4 H), −1.4 (s, 4 H), −10.7 (s, 4 H). MS (ESI$^+$): m/z (%) = 177.624 (11, [dgpy+2H]$^{2+}$), 254.134 (51, [Fe(dgpy)$_2$]$^{3+}$), 354.240 (14, [dgpy+H]$^+$), 453.682 (100, {[Fe(dgpy)$_2$][PF$_6$]}$^{2+}$), 500.212 (95, {[dgpy+2H][PF$_6$]}$^+$), 504.199 (13, {[dgpy+2H][OTf]}$^+$), 1052.329 (80, {[Fe(dgpy)$_2$][PF$_6$]$_2$}$^+$). MS (HR-ESI$^+$): calcd. for $C_{38}H_{54}F_6FeN_{14}P_2^{2+}$: m/z = 453.6818. Found: 453.6817. IR (ATR): $\tilde{\nu}$/cm^{-1} = 2950 (vw), 2876 (vw), 1590 (w), 1574 (vw), 1507 (vw), 1563 (vw), 1444 (vw), 1384 (w), 1364 (vw, sh), 1328 (vw), 1306 (w), 1270 (vw, sh), 1209 (w), 1159 (vw), 1116 (vw), 1102 (vw), 1072 (vw), 1060 (vw), 1043 (vw), 1024 (vw), 945 (vw), 914 (vw), 877 (vw), 827 (vs, PF), 800 (m, sh), 736 (w), 713 (w), 671 (vw), 637 (vw), 610 (vw), 555 (vs, PF$_2$, def.), 516 (vw, sh), 484 (vw), 469 (vw), 418 (w). EPR (PrCN, 77 K): $g_{1,2,3}$ = 2.617, 2.197, 1.768; Δg = 0.849. UV/vis (CH_3CN, 295 K): λ_{max}/nm (ε/M^{-1} cm^{-1}) = 310 (11500), 395 (2140), 462 (3410), 486 (sh, 3330).

RESULTS AND DISCUSSION

Synthesis. The homoleptic iron(II) target complex [Fe(dgpy)$_2$][OTf]$_2$ (**1[OTf]$_2$**) precipitated as a dark red solid from a solution of iron(II) triflate and 2.2 equiv of the ligand dgpy[32] under inert conditions in THF at room temperature (Scheme 1). Its composition was confirmed by elemental analysis, and IR and ^{1}H NMR spectroscopy as well as ESI$^+$ mass spectrometry (Supporting Information, Figures S1−S4). Anion metathesis with [^{n}Bu$_4$N][PF$_6$] formed the corresponding hexafluorophosphate salt **1[PF$_6$]$_2$** (Scheme 1).

Diffusion of diethyl ether into CH_3CN solutions yielded crystals suitable for single-crystal X-ray diffraction analyses.

Scheme 1. Synthesis of Iron(II/III) Complexes with the Ligand dgpy[a]

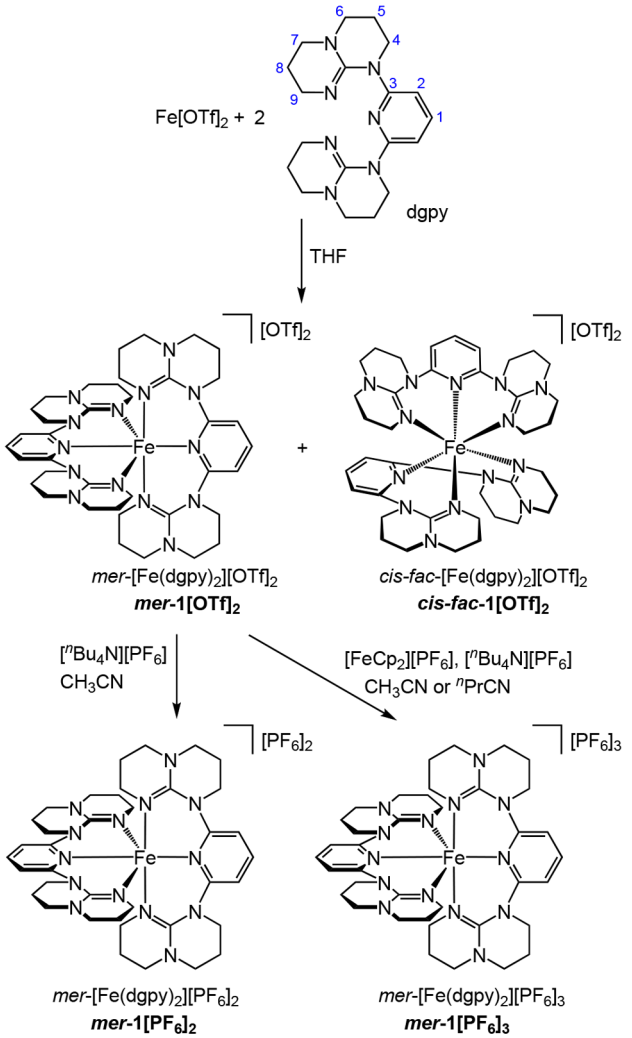

[a]Atom numbering used for NMR assignments is shown in blue.

https://doi.org/10.1021/acs.inorgchem.1c03511
Inorg. Chem. 2022, 61, 1659−1671

Similar to $[Co(dgpy)_2]^{3+}$,[31] yet in contrast to the reported cis-facially coordinated $[Ru(dgpy)_2]^{3+}$ complex (Chart 1),[32] the dgpy ligand coordinates in a meridional fashion in the iron(II) complex ***mer*-1**$^{2+}$ as confirmed by X-ray diffraction analyses of single crystals of $\mathbf{1}[\mathbf{OTf}]_2\times0.5CH_3CN$ ($Pna2_1$; severely disordered guanidine rings in the cation; 173 K) and $\mathbf{1}[\mathbf{PF_6}]_2\times CH_3CN$ (isopointal; $Pna2_1$; 120 K; Figure 1). In

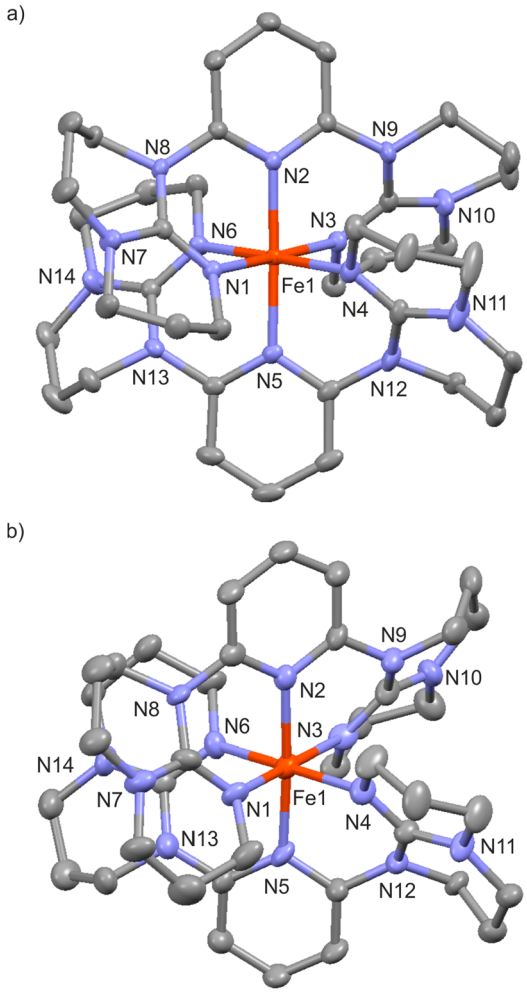

Figure 1. Molecular structures of the cations of a) $\mathbf{1}[\mathbf{PF_6}]_2\times CH_3CN$ (120 K) and b) $\mathbf{1}[\mathbf{PF_6}]_3\times1.5CH_3CN$ (120 K, only one of the two independent cations A/B in the asymmetric unit shown) determined by XRD. Thermal ellipsoids are displayed at 50% probability. Hydrogen atoms are omitted for clarity.

the latter salt, the disorder of the heterocyclohexyl rings of the coordinated dgpy ligands is less severe, and consequently, only the metrical data of this analysis will be discussed in the following.

The Fe−N distances between 1.946−2.007 Å in ***mer*-1**$^{2+}$ at 120 K clearly suggest a low-spin state of iron(II).[67−69] Compared to the isoelectronic low-spin cobalt(III) complex $[Co(dgpy)_2]^{3+}$, the metal−ligand bond lengths are slightly longer due to the lower charge of the central ion. This has also been observed for the $[Fe(ddpd)_2]^{2+}/[Co(ddpd)_2]^{3+}$ pair.[12,34] Fe−N distances of the central pyridine units are smaller than the Fe−N distances of the terminal guanidine moieties (Table 1), similar to the cobalt(III) complex.[31] This M−N distance difference between terminal and central donor atoms is similar to $[M(ddpd)_2]^{n+}$ complexes featuring six-membered chelate rings yet much less pronounced than in $[M(tpy)_2]^{n+}$ complexes with five-membered chelate rings (tpy = 2,2′:6′,2″-terpyridine).[34] Consequently, the $[FeN_6]$ local symmetry of ***mer*-1**$^{2+}$ is much closer to an ideal octahedron with a shape parameter $S(OC\text{-}6)$[70] of 0.08 than $[Fe(tpy)_2]^{2+}$ with a much larger shape parameter of $S(OC\text{-}6) = 1.81$.[34] Although the XRD analyses of single crystals at 120 and 173 K suggest the presence of meridionally coordinated low-spin iron(II) only, spectroscopic studies in solution and in the solid bulk material at different temperatures reveal a higher diversity of relevant iron(II) species in terms of configuration and spin state (vide infra).

Variable Temperature Studies of the Iron(II) Complex. In the ^{1}H NMR spectrum of analytically pure $\mathbf{1}[\mathbf{OTf}]_2$ in CD_3CN at room temperature, the ^{1}H NMR resonances were broad and shifted to lower and higher field strength (+29.3 to −4.4 ppm; Figure 2). Such shifts are characteristic for paramagnetic species, and hence, we suggest the presence of high-spin iron(II) complexes at room temperature. Upon cooling to 183 K in d_6-acetone, these resonances shifted into the diamagnetic region (+10 to 0 ppm; Figures 2 and 3), suggesting a spin crossover to the low-spin iron(II) complex ***mer*-1**$^{2+}$, as observed by XRD at 120 and 173 K. The observed temperature-dependent shifts were fully reversible (Supporting Information, Figure S5).

The appearance of averaged signals instead of separated signals for the high- and low-spin isomers indicates a fast exchange between both spin states as typically observed for iron(II) and cobalt(III) SCO complexes.[71−77] From the line widths of the proton resonances at 31.78, 16.21, and 15.95 ppm (298 K), a high-spin/low-spin exchange constant k_{hl} was estimated around (7.2−30) × 10^5 s^{-1}, a range typically observed for SCO complexes (Supporting Information, Table S1).[67] Yet, other dynamics such as chair-twist boat ring flipping might affect the NMR line widths as well, especially the resonances of the aliphatic protons.

Unexpectedly, a set of 19 clearly discernible, paramagnetically shifted ^{1}H NMR resonances was additionally present (δ = +99 to −66 ppm at 193 K; Figures 2 and 3). These resonances shift almost linearly with temperature (Figure 2; Supporting Information, Figures S5 and S6). With respect to the iron(II) SCO complex ***mer*-1**$^{2+}$, they integrate to less than 20%. The observed large paramagnetic shift confirms a high-spin species, and the number of resonances suggests a much less symmetric structure of this species. A conceivable paramagnetic iron(III) impurity is excluded on the basis of the correct elemental analysis and of the intended preparation and ^{1}H NMR spectroscopic characterization of the iron(III) complex ***mer*-1**$^{3+}$ showing very different ^{1}H NMR resonances (vide infra). As a conceivable trans-facial isomer possesses C_2 symmetry and consequently only a single set of ligand proton resonances, we tentatively assign these broad and shifted resonances to the cis-facial isomer ***cis-fac*-1**$^{2+}$ with C_1 symmetry. This complex possesses a high-spin electronic ground state down to 183 K. In the temperature range 247−193 K, the ^{1}H NMR resonances of ***cis-fac*-1**$^{2+}$ are clearly visible and integrable (Figure 2). The relative integrals of resonances of ***mer*-1**$^{2+}$ and ***cis-fac*-1**$^{2+}$ are temperature-independent suggesting that the relative amounts do not significantly change with temperature, and hence, equilibration of the isomers is unlikely.

The *mer* and *cis-fac* isomers of **1**$^{2+}$ reproducibly formed during the synthetic procedure. Yet, attempts to separate *cis-fac* and *mer* isomers by crystallization of the bulk material failed.

https://doi.org/10.1021/acs.inorgchem.1c03511
Inorg. Chem. 2022, 61, 1659−1671

Table 1. Selected Bond Lengths/Å and Angles/deg of the Cations of $1[PF_6]_2 \times CH_3CN$ (120 K) and $1[PF_6]_3 \times 1.5CH_3CN$ (120 K, Two Independent Cations A/B in the Asymmetric Unit) Obtained by XRD and of *mer*-1^{2+} (Low-Spin), *mer*-1^{2+} (High-Spin), *cis-fac*-1^{2+} (High-Spin), and *mer*-1^{3+} (Low-Spin) Obtained by DFT Calculations

	XRD			DFT			
	$1[PF_6]_2$	$1[PF_6]_3$ (A)	$1[PF_6]_3$ (B)	low-spin *mer*-1^{2+}	high-spin *mer*-1^{2+}	high-spin *cis-fac*-1^{2+}	low-spin *mer*-1^{3+}
M1−N1	2.001(2)	1.93(1)	1.95(1)	2.010	2.145	2.151	1.952
M1−N2	1.959(2)	1.96(1)	1.96(1)	1.981	2.176	2.240	1.975
M1−N3	1.996(2)	1.98(1)	1.97(1)	2.008	2.151	2.145	1.993
M1−N4	1.999(2)	1.97(1)	1.94(1)	2.025	2.167	2.151	1.947
M1−N5	1.946(2)	1.95(1)	1.95(1)	1.982	2.173	2.272	1.969
M1−N6	2.007(2)	1.93(1)	1.96(1)	2.011	2.157	2.174	1.997
N1−Fe1−N2	89.23(8)	88.7(4)	89.0(4)	87.8	82.0	78.3	88.8
N2−Fe1−N3	89.25(9)	90.1(4)	90.5(4)	88.5	82.8	80.1	88.3
N4−Fe1−N5	89.04(8)	90.3(4)	88.8(4)	87.5	81.1	79.4	88.3
N5−Fe1−N6	88.53(8)	87.6(4)	90.9(4)	88.1	81.4	78.4	87.9
S(OC-6)	0.08	0.15	0.08	0.13	1.51	1.25	0.12

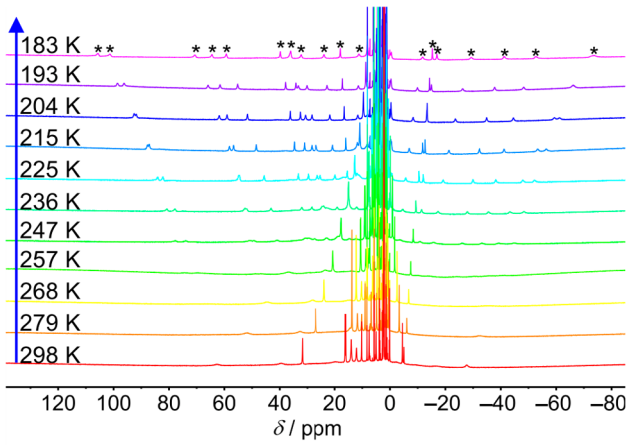

Figure 2. Variable temperature ^{1}H NMR spectra of $1[OTf]_2$ in d_6-acetone (cooling). Eighteen resonances of the *cis-fac* isomer are marked with asterisks in the spectrum at 183 K, and two resonances are superimposed in the spectrum at 183 K but visible in the spectrum at 193 K, leading to 19 discernible resonances.

Consequently, we take into account a constant amount of high-spin *cis-fac*-1^{2+} being present in the bulk material of *mer*-1^{2+} in the following discussion—in addition to the temperature-dependent SCO behavior of *mer*-1^{2+}.

Applying Evans' method[78−80] in deuterated acetone at variable temperature to determine the magnetic properties in solution and accounting for the presence of high-spin *cis-fac*-1^{2+} yields the $\Delta\nu$ T vs T plot of *mer*-1^{2+} depicted in Figure 4 (Supporting Information, Figures S8 and S9). The thus obtained experimental magnetic data were fit to a distribution between the low-spin and high-spin complexes without taking into account any cooperativity giving ΔH = 29.6(8) kJ mol^{-1} and ΔS = 110(3) J mol^{-1} K^{-1}. The spin-transition temperature $T_{1/2}$ = 269 K with 50% low- and 50% high-spin fractions is close to room temperature. At room temperature (293 K), 75% of the *mer*-1^{2+} complexes are in the high-spin state. From the higher degeneracy of the high-spin state ($^5T_2$; 15 microstates) compared to the low-spin state ($^1A_1$; 1 microstate), the theoretical entropic gain amounts to $\Delta S_{el} = R \ln(\Omega_{high\text{-}spin}/\Omega_{low\text{-}spin}) = R \ln(15/1)$ = 22.5 J mol^{-1} K^{-1}. If the orbital degeneracy of the high-spin state is significantly lifted, the electronic contribution to the entropy amounts to only $\Delta S_{el} = R \ln(\Omega_{high\text{-}spin}/\Omega_{low\text{-}spin}) = R \ln(5/1)$ = 13.4 J mol^{-1} K^{-1}.[81] Consequently, the major entropy gain ΔS_{vib} (80−88%) results from higher vibrational degrees of freedom of the high-spin state. The larger DFT calculated bond lengths of the high-spin state (high-spin *mer*-1^{2+}) as compared to low-spin *mer*-1^{2+} reflect this structural and vibrational contribution (Table 1).

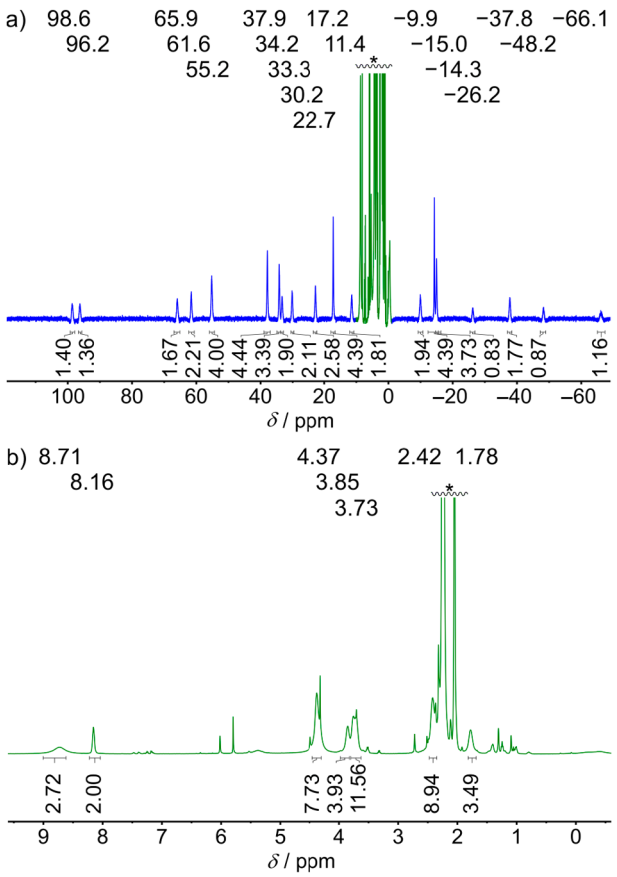

Figure 3. a) ^{1}H NMR spectrum of $1[OTf]_2$ in d_6-acetone at 193 K. Resonances of the *cis-fac* isomer are colored blue. b) Zoom into the diamagnetic region of the ^{1}H NMR spectrum at 193 K showing the resonances of low-spin *mer*-1^{2+} in green. Unassigned resonances can be attributed to diamagnetic impurities such as residual solvents and grease.

The bulk material of $1[OTf]_2$ at 293 K is thus composed of approximately 61% high-spin *mer*-1^{2+}, 20% low-spin *mer*-1^{2+}, and 19% high-spin *cis-fac*-1^{2+}. The absorption spectrum of

https://doi.org/10.1021/acs.inorgchem.1c03511
Inorg. Chem. 2022, 61, 1659−1671

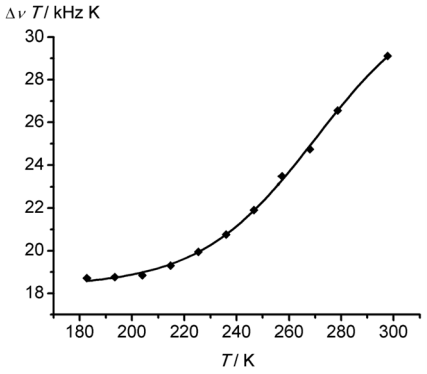

Figure 4. $\Delta\nu\ T$ vs T data obtained from ^{1}H NMR measurements of $\mathbf{1}[\mathbf{OTf}]_2$ using Evans' method in d_6-acetone and fit according to $R \ln K = -\Delta H/T + \Delta S$ using $\Delta H = 29.6(8)$ kJ mol^{-1} and $\Delta S = 110(3)$ J mol^{-1} K^{-1}.

$\mathbf{1}[\mathbf{OTf}]_2$ dissolved in CH_3CN at 293 K (Figure 5) showed absorption bands at 222, 255, and 302 nm assigned to mainly ligand-based transitions and three maxima in the visible spectral region at 466, 530, and 582 nm assigned to MLCT transitions. Time-dependent DFT calculations ((CPCM-(acetonitrile)-RIJCOSX-B3LYP-D3BJ-ZORA/def2-TZVP))

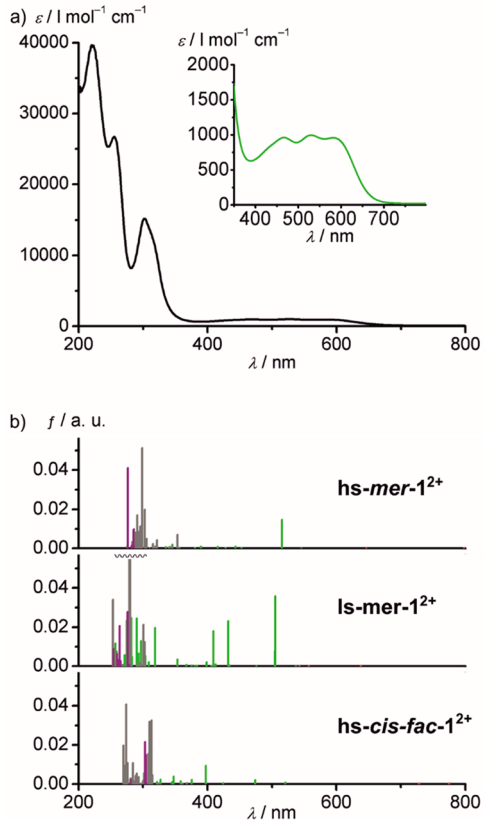

Figure 5. a) UV/vis spectrum of $\mathbf{1}[\mathbf{OTf}]_2$ in acetonitrile at 293 K. The inset shows a zoom into the MLCT region. b) TDDFT calculated transitions of high-spin ***mer*-1^{2+}**, low-spin ***mer*-1^{2+}**, and high-spin ***cis-fac*-1^{2+}**, respectively, with the color code indicating the character of the transition according to charge-transfer number analyses (green: MLCT, gray: ILCT/LC, purple: LL′CT; the oscillator strengths of the MC states are too small to be visible on this scale; Supporting Information, Figures S10−S12).

on high-spin ***mer*-1^{2+}**, low-spin ***mer*-1^{2+}**, and high-spin ***cis-fac*-1^{2+}** cations predicted MLCT transitions in the correct energy region at 515, 505, and 474 nm, respectively (Figure 5). Weak spin-allowed metal-centered transitions for the low- and high-spin complexes (^{1}MC of low-spin ***mer*-1^{2+}**: 542, 557, 638 nm; ^{5}MC of high-spin ***mer*-1^{2+}**: 545, 646 nm; ^{5}MC of high-spin ***cis-fac*-1^{2+}**: 728, 775 nm) have been identified at even lower energy in all cases by the quantum chemical calculations and the corresponding analysis of the charge-transfer numbers (Supporting Information, Figures S10−S12).

Upon cooling to 160 K in butyronitrile, the intensity of the ligand-centered UV bands and the low-energy MLCT bands increased (Figure 6a). Rewarming to 300 K restores the

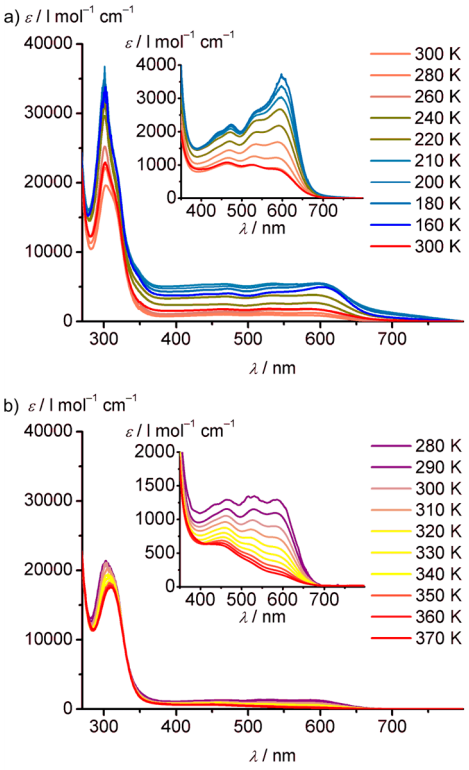

Figure 6. Variable temperature UV/vis spectra of $\mathbf{1}[\mathbf{OTf}]_2$ in butyronitrile: a) during cooling from 300 to 160 K and rewarming to 300 K and b) during warming from 280 to 370 K. Figure S13 (Supporting Information) displays the respective differential UV/vis spectra.

spectrum confirming reversibility (Figure 6a). Furthermore, the pattern of the MLCT bands changed as the low-energy MLCT band increased much stronger at low temperature (Figure 6a). Upon heating to 370 K, the lowest energy MLCT band almost bleached (Figure 6b). The observed band pattern at low temperature resembles the TDDFT calculated pattern of low-spin ***mer*-1^{2+}** (Figures 5b and 6a). Fitting the absorbance at 540 nm vs temperature (in butyronitrile) with a distribution between the low- and high-spin complexes without taking into account any cooperativity gives $\Delta H = 30(1)$ kJ mol^{-1} and $\Delta S = 107(3)$ J mol^{-1} K^{-1} (Supporting Information, Figure S14a) in very good agreement with the thermodynamic parameters obtained from the paramagnetically shifted ^{1}H NMR solvent resonances in acetone (Supporting Information, Figures S8 and S9). The temperature-dependent optical characteristics of **1^{2+}** in acetone indeed

https://doi.org/10.1021/acs.inorgchem.1c03511
Inorg. Chem. 2022, 61, 1659−1671

match those measured in butyronitrile (Supporting Information, Figure S14b), confirming that the solvent plays no significant role for the relative stability of high- and low-spin states of ***mer*-1**$^{2+}$.

In order to probe for potential cooperative effects in the solid state, the χT product of solid **1**$[OTf]_2$ was measured using a SQUID magnetometer. Cooling the sample to 150 K and rewarming to 350 K revealed a gradual SCO without any hysteresis (Supporting Information, Figure S15). Taking into account the presence of the high-spin ***cis-fac*-1**$^{2+}$ isomer gave a fit of the χT vs T curve with ΔH = 25.2(9) kJ mol^{-1} and ΔS = 88(3) J mol^{-1} K^{-1} (Figure 7). These values compare well to

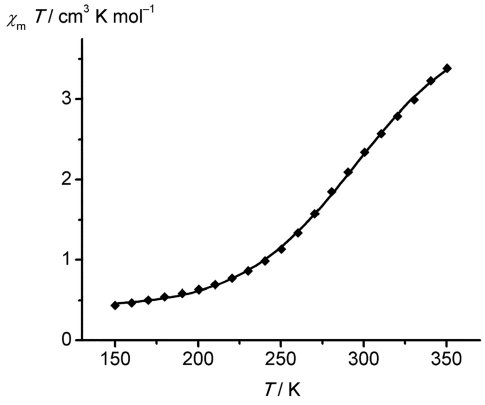

Figure 7. χT vs T data obtained from magnetic susceptibility measurements of ***mer*-1**$[OTf]_2$ using a SQUID magnetometer and fit according to $R \ln K = -\Delta H/T + \Delta S$ using ΔH = 25.2(9) kJ mol^{-1} and ΔS = 88(3) J mol^{-1} K^{-1}. The residual magnetic susceptibility at low temperature arises from the presence of high-spin [***cis-fac*-1**][OTf]$_2$.

the data obtained from NMR and optical spectroscopy in solution. They also document that cooperativity between the ***mer*-1**$^{2+}$ cations is absent both in solution and in the solid state and that the environment has no significant impact on the relative stability of high- and low-spin ***mer*-1**$^{2+}$.

^{57}Fe Mössbauer spectra of **1**$[OTf]_2$ at selected temperatures are shown in Figure 8, and individual hyperfine parameters are given in Table 2. The low-temperature spectra were well fitted by two principle subspectra referring to each spin configuration (low-spin and high-spin), providing the center shift (CS), quadrupole splitting (QS), and the Gaussian width of the quadrupole splitting distribution (σ_{QS}). At approximately 250 K, the line widths of each subspectrum broadened and additional contributions appeared at the foothills of the respective absorption lines, as typically found in dynamic scenarios. These additional subspectra represent the species arising from the low-spin and high-spin states, respectively. The modeling followed the two center shifts resembling the main high-spin and low-spin contributions. Importantly, strongly diverging quadrupole splittings were evident with increasing temperature. We assign these developing features to the dynamic part of the transformation (high-spin-dyn and low-spin-dyn).

Having established the SCO behavior of **1**$^{2+}$ in solution and in the solid state, we probed potential luminescence properties of the high- and low-spin complexes at room temperature and at 77 K in butyronitrile, respectively. However, no emission could be detected after excitation at wavelengths between 190 and 605 nm with our equipment. This finding agrees with the

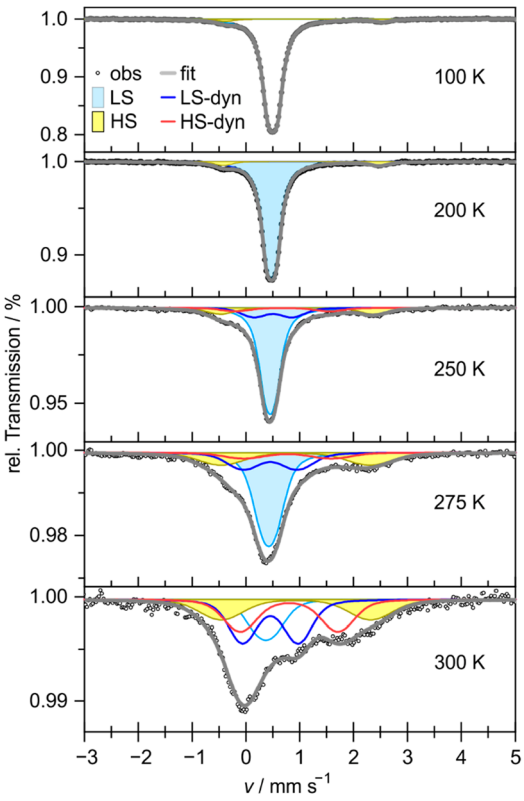

Figure 8. ^{57}Fe Mössbauer spectra of **1**$[OTf]_2$ taken at the indicated temperatures. Deconvoluted subspectra are indicated.

Table 2. ^{57}Fe Mössbauer Hyperfine Parameters (Center Shift (CS), Quadrupole Splitting (QS), Gaussian Width of the Quadrupole Splitting Distribution (σ_{QS})) and Site Populations of 1$[OTf]_2$ at Selected Temperatures

T/K	site	CS/ mm s^{-1}	QS/ mm s^{-1}	σ_{QS}/ mm s^{-1}	site populations /%
300	ls	0.37(1)	0.3(1)	0.4(2)	18(1)
	ls-dyn	0.46(1)	1.03(5)	0.40(5)	32(1)
	hs	0.93(1)	2.8(1)	0.7(1)	23(1)
	hs-dyn	0.80(1)	1.82(6)	0.50(6)	27(1)
275	ls	0.43(1)	0.25(3)	0.26(5)	50(1)
	ls-dyn	0.45(1)	1.01(5)	0.49(8)	20(1)
	hs	0.92(1)	2.76(9)	0.72(9)	21(1)
	hs-dyn	0.77(1)	1.6(2)	0.6(2)	9(1)
250	ls	0.45(1)	0.17(1)	0.13(2)	68(1)
	ls-dyn	0.51(1)	0.72(3)	0.34(6)	12(1)
	hs	0.95(1)	2.84(6)	0.41(6)	14(1)
	hs-dyn	0.68(1)	1.8(1)	0.4(1)	6(1)
200	ls	0.47(1)	0.16(1)	0.04(1)	93.9(5)
	hs	1.03(1)	2.89(4)	0.21(5)	6.1(5)
100	ls	0.50(1)	0.17(1)	0.06(1)	96.1(3)
	hs	1.08(2)	2.92(4)	0.19(6)	3.9(3)

presence of low-energy MC states, which enable efficient nonradiative decay (Supporting Information, Figures S10–S12).

Redox Chemistry. The bulk material **1**$[OTf]_2$ dissolved in CH_3CN with [^{n}Bu$_4$N][PF$_6$] as a supporting electrolyte showed a quasi-reversible oxidation wave at +0.97 V vs ferrocene (Figure 9; Supporting Information, Figure S16) assigned to the oxidation of the coordinated dgpy ligand. A reversible

https://doi.org/10.1021/acs.inorgchem.1c03511
Inorg. Chem. 2022, 61, 1659−1671

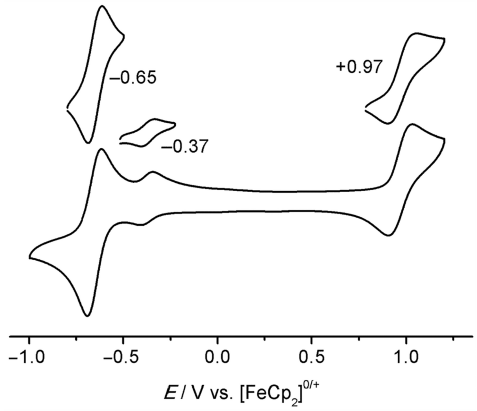

Figure 9. Cyclic voltammogram of $\mathbf{1}[\mathbf{OTf}]_2$, 1 mM in acetonitrile containing 0.1 M $[^nBu_4N][PF_6]$ as the supporting electrolyte.

oxidation was observed at −0.65 V vs ferrocene and assigned to the $Fe^{II/III}$ redox couple of ***mer*-1**$^{2+}$/***mer*-1**$^{3+}$. For comparison, the $[M(dgpy)_2]^{2+/3+}$ couple appeared at −0.69 V vs ferrocene (M = Ru; *cis-fac* isomer)[32,82] and at −0.98 V (M = Co; *mer* isomer).[31,82] A reversible smaller wave is visible in the cyclic and square wave voltammograms at −0.37 V vs ferrocene. Uncoordinated dgpy is irreversibly oxidized at +0.37 V under the same conditions, thus excluding ligand dissociation under the oxidative conditions. The ratio of the peak currents of the waves at −0.37 V and −0.65 V amounts to approximately 20% (Figure 9). As we have already assigned an approximately 19% amount of the sample to the high-spin ***cis-fac*-1**$^{2+}$ isomer, we attribute this wave to the $Fe^{II/III}$ redox couple of the high-spin ***cis-fac*-1**$^{2+}$ isomer.

The negative $Fe^{II/III}$ redox potentials enable oxidation of both isomers to the respective iron(III) complexes by dioxygen or by ferrocenium salts. Addition of 1 equiv of $[FeCp_2][PF_6]$ to a solution of $\mathbf{1}[\mathbf{OTf}]_2$ yielded **1**$^{3+}$ (Scheme 1, Figures S17−S20). Structure analysis of a single crystal of **1**-$[\mathbf{PF_6}]_3\times1.5CH_3CN$ by XRD confirmed the meridional coordination of the dgpy ligands (Figure 1). Although the asymmetric unit contains two independent cations and three disordered PF_6^- counterions which leads to a poor bond precision, the low-spin state of the iron(II) center could be confirmed based on the short Fe−N distances (Table 1). The Fe−N bond lengths are further substantiated by DFT calculations on low-spin ***mer*-1**$^{3+}$ (Table 1). The ^{1}H NMR spectrum of **1**$^{3+}$ shows resonances strongly shifted to lower or higher fields (δ = +54 to −11 ppm; Figure 10a; Supporting Information, Figure S17). The number of observed resonances fits to a C_2-symmetric complex ***mer*-1**$^{3+}$. Using only 0.5 equiv of the oxidant $[FeCp_2][PF_6]$ instead of 1.0 equiv resulted in separate signal sets for the iron(III) complex ***mer*-1**$^{3+}$ and the (mainly high-spin) iron(II) complex ***mer*-1**$^{2+}$ (Figure 10a). This indicates a rather slow electron exchange between ***mer*-1**$^{2+}$ and ***mer*-1**$^{3+}$ on the ^{1}H NMR time scale (400 MHz) at room temperature.

In the X-band EPR spectrum of $\mathbf{1}[\mathbf{OTf}]_2$ and 1 equiv of $[FeCp_2][PF_6]$ in frozen butyronitrile solution, a rhombic EPR resonance appeared with $g_{1,2,3}$ = 2.617, 2.197, 1.768 (77 K; Figure 10b; Supporting Information, Figure S18). This pattern is characteristic for pseudo-octahedral low-spin iron(III) complexes, e.g., with $g_{1,2,3}$ = 2.490, 2.296, 1.815 and $g_{1,2,3}$ = 2.821, 2.247, 1.561 reported for low-spin $[Fe(ddpd)_2]^{3+}$ and $[Fe(dcpp)(ddpd)]^{3+}$, respectively.[12] The *g*-anisotropy of **1**$^{3+}$

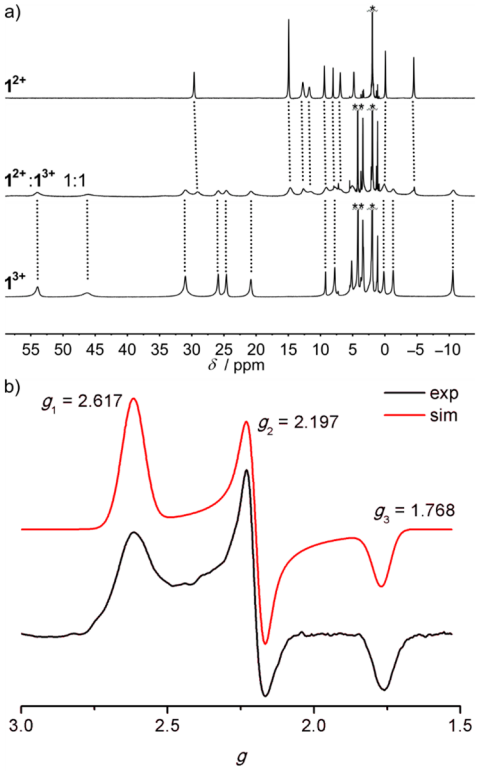

Figure 10. a) ^{1}H NMR spectra of $\mathbf{1}[\mathbf{OTf}]_2$ in CD_3CN at room temperature without and with 0.5 and 1 equiv of $[FeCp_2][PF_6]$ added; dotted lines correlate resonances of the spectra of **1**$^{2+}$ and **1**$^{3+}$ with the spectrum of the mixture; * denotes acetonitrile, ** denotes ferrocene; b) baseline-corrected X-band EPR spectrum (black) of $\mathbf{1}[\mathbf{OTf}]_2$ with 1 equiv of $[FeCp_2][PF_6]$ added in butyronitrile at 77 K and simulated spectrum (red).

with $\Delta g = g_1 - g_3$ = 0.849 is in between that of the homoleptic complex $[Fe(ddpd)_2]^{3+}$ (Δg = 0.675) and the heteroleptic complex $[Fe(dcpp)(ddpd)]^{3+}$ (Δg = 1.26).[12] Contributions of a conceivable minor Fe^{III} species ***cis-fac*-1**$^{3+}$ are not discernible. Several reasons might account for this absence. The amount of ***cis-fac*-1**$^{3+}$ could be too small to be detectable, the *g*-tensor of ***cis-fac*-1**$^{3+}$ could be similar to that of ***mer*-1**$^{3+}$, ***cis-fac*-1**$^{3+}$ could have isomerized to ***mer*-1**$^{3+}$, or ***cis-fac*-1**$^{3+}$ could be an EPR-silent high-spin complex due to the weaker ligand field strength of facially coordinated dgpy. With the data at hand, this cannot be decided.

Electrochemical or chemical oxidation of $\mathbf{1}[\mathbf{OTf}]_2$ bleaches the MLCT band at 582 nm and gives rise to a 462 nm band with a shoulder around 500 nm (Supporting Information, Figure S22, Figure 11a). TDDFT calculations and charge-transfer number analysis[65,66] assign the ^{2}LMCT character from the electron-rich guanidine moieties to the electron-deficient iron(III) center to these absorption bands (Figure 11b). Several less intense MC transitions are located at even lower energy (Supporting Information, Figure S21). In contrast to the fluorescent hexacarbene iron(III) complexes $[Fe(btz)_3]^{3+}$ and $[Fe(phtmeimb)_2]^+$,[29,30] excitation of ***mer*-1**$^{3+}$ at wavelengths between 398 and 485 nm in dry butyronitrile did not result in observable ^{2}LMCT fluorescence, neither at room temperature in fluid solution nor at 77 K in frozen solution. This is likely due to the presence of these low-energy ^{2}MC states, which enable nonradiative deactivation of the excited states.[83]

https://doi.org/10.1021/acs.inorgchem.1c03511
Inorg. Chem. 2022, 61, 1659−1671

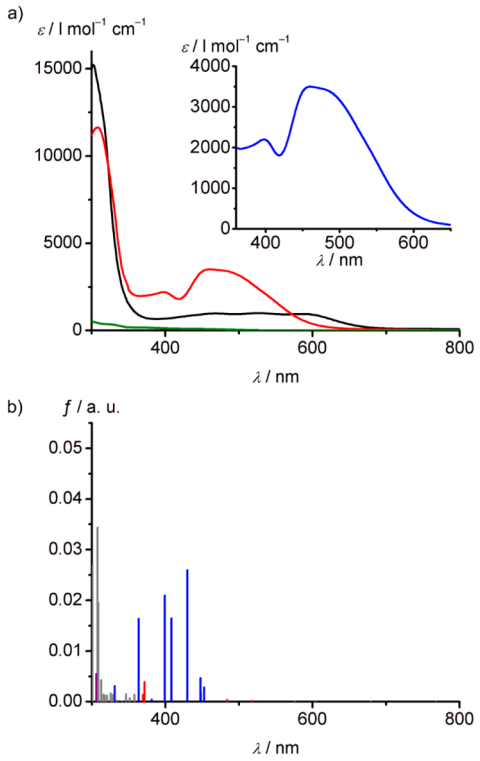

Figure 11. a) UV/vis spectrum of $\mathbf{1}[\mathbf{OTf}]_2$ before (black) and after (red) oxidation with 1 equiv of $[FeCp_2][PF_6]$; UV/vis spectrum of $[FeCp_2]$ in green at 300 K for comparison. b) TDDFT calculated transitions of low-spin ***mer*-1**$^{3+}$ with the color code indicating the character of the transition according to charge-transfer analyses (red: MC, blue: LMCT, gray: ILCT/LC, purple: LL′CT. The oscillator strengths of the MC states in red are hardly visible on this scale; Supporting Information, Figure S21).

Although we are aware that the relative energy of low- and high-spin states calculated by DFT methods critically depends on the exact exchange[84,85] and that the B3LYP functional artificially favors the high-spin state,[86] we note that the Gibbs free enthalpy difference at 298 K between low- and high-spin ***mer*-1**$^{2+}$ calculated by DFT (B3LYP) ($\Delta G_{298,mer,\mathrm{DFT}}$ = −36 kJ mol^{-1} favoring the high-spin at this temperature) is much smaller than that for low- and high-spin ***cis-fac*-1**$^{2+}$ ($\Delta G_{298,cis\text{-}\mathrm{fac}}$ = −67 kJ mol^{-1}) in agreement with the SCO behavior of ***mer*-1**$^{2+}$ ($\Delta G_{298,mer,\mathrm{exp}}$ = −3 kJ mol^{-1} from the thermodynamic data in solution) and the high-spin character of ***cis-fac*-1**$^{2+}$. Conceivable low- and high-spin ***trans-fac*-1**$^{2+}$ isomers are unfavorable compared to low-spin ***mer*-1**$^{2+}$ by 52 kJ mol^{-1} and to high-spin ***cis-fac*-1**$^{2+}$ by 39 kJ mol^{-1}, respectively. We also note that the calculated difference in electronic energies favors the high-spin state of ***mer*-1**$^{2+}$ by only −10 kJ mol^{-1}. Consequently, the DFT calculations correctly predict SCO behavior, high-spin character, and a high energy for the ***mer*-1**$^{2+}$, ***cis-fac*-1**$^{2+}$, and ***trans-fac*-1**$^{2+}$ isomers, respectively. TDDFT calculations describe the CT absorption band patterns of **1**$^{2+}$ and **1**$^{3+}$ (spin-allowed MLCT, LL′CT/ILCT, LMCT; Supporting Information, Figures S10−S12, S21) qualitatively correct. Furthermore, MC excited states (with the same multiplicity as the ground state) are lower in energy than the charge-transfer states in all cases. This MC < CT ordering likely applies to states of different multiplicity than the ground state as well, namely the triplet (and quintet) MC excited states of low-spin **1**$^{2+}$ and the quartet MC states of low-spin **1**$^{3+}$, explaining the absence of CT luminescence.

CONCLUSION

The donor−acceptor ligand dgpy preferably coordinates to iron(II) in a meridional fashion giving *mer*-$[Fe(dgpy)_2]^{2+}$ (***mer*-1**$^{2+}$), while a cis-facial isomer ***cis-fac*-1**$^{2+}$ is present in lower amounts. The ligand field strength in the meridional coordination mode is higher than in the cis-facial coordination mode, resulting in SCO behavior of ***mer*-1**$^{2+}$ and a high-spin state of ***cis-fac*-1**$^{2+}$. Low-spin ***mer*-1**$^{2+}$, high-spin ***mer*-1**$^{2+}$, and high-spin ***cis-fac*-1**$^{2+}$ exhibit ^{1}MLCT/^{5}MLCT absorption bands in the visible spectral region (Figure 5; Supporting Information, Figure S23). The room temperature composition of a solution of **1**$^{2+}$ yields a nearly constant panchromatic absorption from 400 to 600 nm. In spite of the low-energy MLCT states and the comparably high ligand field strength in the meridional coordination mode, MC excited states are lower in energy than the $^{1/3}$MLCT states, and consequently, luminescence is not observed. Oxidation of ***mer*-1**$^{2+}$ gives the low-spin complex ***mer*-1**$^{3+}$ with ^{2}LMCT absorption bands around 460−500 nm. In spite of the high ligand field strength of the iron(III) complex, MC excited states of ***mer*-1**$^{3+}$ are still lower in energy than the CT states preventing fluorescence from the ^{2}LMCT states.

ASSOCIATED CONTENT

Supporting Information

The Supporting Information is available free of charge at https://pubs.acs.org/doi/10.1021/acs.inorgchem.1c03511.

Detailed NMR, IR, ESI$^+$, EPR, UV/vis, SQUID, and electrochemical data, fitting procedures, information on computational studies including charge-transfer number analyses, difference densities, and Cartesian coordinates of optimized geometries (PDF)

Accession Codes

CCDC 2059034 and 2062796−2062797 contain the supplementary crystallographic data for this paper. These data can be obtained free of charge via www.ccdc.cam.ac.uk/data_request/cif, or by emailing data_request@ccdc.cam.ac.uk, or by contacting The Cambridge Crystallographic Data Centre, 12 Union Road, Cambridge CB2 1EZ, UK; fax: +44 1223 336033.

AUTHOR INFORMATION

Corresponding Author

Katja Heinze − *Department of Chemistry, Johannes Gutenberg University, 55128 Mainz, Germany*; orcid.org/0000-0003-1483-4156; Email: katja.heinze@uni-mainz.de

Authors

Johannes Moll − *Department of Chemistry, Johannes Gutenberg University, 55128 Mainz, Germany*

Christoph Förster − *Department of Chemistry, Johannes Gutenberg University, 55128 Mainz, Germany*

Alexandra König − *Department of Chemistry, Johannes Gutenberg University, 55128 Mainz, Germany*

Luca M. Carrella − *Department of Chemistry, Johannes Gutenberg University, 55128 Mainz, Germany*

Manfred Wagner − *Max Planck Institute for Polymer Research, 55128 Mainz, Germany*

Martin Panthöfer − *Department of Chemistry, Johannes Gutenberg University, 55128 Mainz, Germany*

https://doi.org/10.1021/acs.inorgchem.1c03511
Inorg. Chem. 2022, 61, 1659−1671

Angela Möller − *Department of Chemistry, Johannes Gutenberg University, 55128 Mainz, Germany*
Eva Rentschler − *Department of Chemistry, Johannes Gutenberg University, 55128 Mainz, Germany;* orcid.org/0000-0003-1431-3641

Complete contact information is available at: https://pubs.acs.org/10.1021/acs.inorgchem.1c03511

Author Contributions

The manuscript was written through contributions of all authors. All authors have given approval to the final version of the manuscript.

Notes

The authors declare no competing financial interest.

■ ACKNOWLEDGMENTS

Financial support from the Deutsche Forschungsgemeinschaft [Priority Program SPP 2102 "Light-controlled reactivity of metal complexes" (HE 2778/14-1)] is gratefully acknowledged (K.H.). Parts of this research were conducted using the supercomputer MOGON and advisory services offered by Johannes Gutenberg University Mainz (https://www.hpc.uni-mainz.de) and the supercomputer Elwetritsch and advisory services offered by the TU Kaiserslautern (https://elwe.rhrk.uni-kl.de), which are members of the AHRP and the Gauss Alliance e.V. A.M. acknowledges support from the Carl-Zeiss Foundation. We thank Prof. Tanja Weil (Max Planck Institute for Polymer Research, Mainz, Germany) for NMR support. We thank Dr. Dieter Schollmeyer for collecting the XRD data of $\mathbf{1}[\mathbf{PF_6}]_2 \times CH_3CN$ and $\mathbf{1}[\mathbf{PF_6}]_3 \times 1.5CH_3CN$.

■ REFERENCES

(1) *Spin crossover in transition metal compounds I*; Gütlich, P., Goodwin, H. A., Eds.; Topics in Current Chemistry 233; Springer: Berlin/Heidelberg, 2004; DOI: 10.1007/b40394-9.
(2) *Spin Crossover in Transition Metal Compounds II*; Gütlich, P., Goodwin, H. A., Eds.; Topics in Current Chemistry 234; Springer: Berlin/Heidelberg, 2004; DOI: 10.1007/b93641.
(3) *Spin Crossover in Transition Metal Compounds III*; Gütlich, P., Goodwin, H. A., Eds.; Topics in Current Chemistry 235; Springer: Berlin/Heidelberg, 2004; DOI: 10.1007/b96439.
(4) Weber, B. Spin crossover complexes with N_4O_2 coordination sphere - The influence of covalent linkers on cooperative interactions. *Coord. Chem. Rev.* **2009**, *253*, 2432−2449.
(5) Halcrow, M. A. The spin-states and spin-transitions of mononuclear iron(II) complexes of nitrogen-donor ligands. *Polyhedron* **2007**, *26*, 3523−3576.
(6) Halcrow, M. A. Iron(II) complexes of 2,6-di(pyrazol-1-yl)pyridines - A versatile system for spin-crossover research. *Coord. Chem. Rev.* **2009**, *253*, 2493−2514.
(7) Decurtins, S.; Gütlich, P.; Hasselbach, K. M.; Hauser, A. W.; Spiering, H. Light-Induced Excited-Spin-State Trapping in Iron(II) Spin-Crossover Systems. Optical Spectroscopic and Magnetic Susceptibility Study. *Inorg. Chem.* **1985**, *24*, 2174−2178.
(8) Decurtins, S.; Gütlich, P.; Köhler, C. P.; Spiering, H.; Hauser, A. W. Light-induced excited spin state trapping in a transition-metal complex: The hexa-1-propyltetrazole-iron(II) tetrafluoroborate spin-crossover system. *Chem. Phys. Lett.* **1984**, *105*, 1−4.
(9) McCusker, J. K.; Walda, K. N.; Dunn, R. C.; Simon, J. D.; Magde, D.; Hendrickson, D. N. Subpicosecond ^{1}MLCT → $^5T_2$ intersystem crossing of low-spin polypyridyl ferrous complexes. *J. Am. Chem. Soc.* **1993**, *115*, 298−307.
(10) Jamula, L. L.; Brown, A. M.; Guo, D.; McCusker, J. K. Synthesis and Characterization of a High-Symmetry Ferrous Polypyridyl Complex: Approaching the $^5T_2/^3T_1$ Crossing Point for Fe^{II}. *Inorg. Chem.* **2014**, *53*, 15−17.
(11) Britz, A.; Gawelda, W.; Assefa, T. A.; Jamula, L. L.; Yarranton, J. T.; Galler, A.; Khakhulin, D.; Diez, M.; Harder, M.; Doumy, G.; March, A. M.; Bajnóczi, É.; Németh, Z.; Pápai, M.; Rozsályi, E.; Sárosiné Szemes, D.; Cho, H.; Mukherjee, S.; Liu, C.; Kim, T. K.; Schoenlein, R. W.; Southworth, S. H.; Young, L.; Jakubikova, E.; Huse, N.; Vankó, G.; Bressler, C.; McCusker, J. K. Using Ultrafast X-ray Spectroscopy To Address Questions in Ligand-Field Theory: The Excited State Spin and Structure of $[Fe(dcpp)_2]^{2+}$. *Inorg. Chem.* **2019**, *58*, 9341−9350.
(12) Mengel, A. K. C.; Förster, C.; Breivogel, A.; Mack, K.; Ochsmann, J. R.; Laquai, F.; Ksenofontov, V.; Heinze, K. A Heteroleptic Push−Pull Substituted Iron(II) Bis(tridentate) Complex with Low-Energy Charge-Transfer States. *Chem. - Eur. J.* **2015**, *21*, 704−714.
(13) Wenger, O. S. Is Iron the New Ruthenium? *Chem. - Eur. J.* **2019**, *25*, 6043−6052.
(14) Hockin, B. M.; Li, C.; Robertson, N.; Zysman-Colman, E. Photoredox catalysts based on earth-abundant metal complexes. *Catal. Sci. Technol.* **2019**, *9*, 889−915.
(15) Lindh, L.; Chábera, P.; Rosemann, N. W.; Uhlig, J.; Wärnmark, K.; Yartsev, A.; Sundström, V.; Persson, P. Photophysics and Photochemistry of Iron Carbene Complexes for Solar Energy Conversion and Photocatalysis. *Catalysts* **2020**, *10*, 315.
(16) Duchanois, T.; Liu, L.; Pastore, M.; Monari, A.; Cebrián, C.; Trolez, Y.; Darari, M.; Magra, K.; Francés-Monerris, A.; Domenichini, E.; Beley, M.; Assfeld, X.; Haacke, S.; Gros, P. C. NHC-Based Iron Sensitizers for DSSCs. *Inorganics* **2018**, *6*, 63.
(17) Arias-Rotondo, D. M.; McCusker, J. K. The photophysics of photoredox catalysis: a roadmap for catalyst design. *Chem. Soc. Rev.* **2016**, *45*, 5803−5820.
(18) Chábera, P.; Kjær, K. S.; Prakash, O.; Honarfar, A.; Liu, Y.; Fredin, L. A.; Harlang, T. C. B.; Lidin, S.; Uhlig, J.; Sundström, V.; Lomoth, R.; Persson, P.; Wärnmark, K. Fe^{II} Hexa *N*-Heterocyclic Carbene Complex with a 528 ps Metal-to-Ligand Charge-Transfer Excited-State Lifetime. *J. Phys. Chem. Lett.* **2018**, *9*, 459−463.
(19) Fredin, L. A.; Pápai, M.; Rozsályi, E.; Vankó, G.; Wärnmark, K.; Sundström, V.; Persson, P. Exceptional Excited-State Lifetime of an Iron(II)-*N*-Heterocyclic Carbene Complex Explained. *J. Phys. Chem. Lett.* **2014**, *5*, 2066−2071.
(20) Harlang, T. C. B.; Liu, Y.; Gordivska, O.; Fredin, L. A.; Ponseca, C. S., JR; Huang, P.; Chábera, P.; Kjær, K. S.; Mateos, H.; Uhlig, J.; Lomoth, R.; Wallenberg, R.; Styring, S.; Persson, P.; Sundström, V.; Wärnmark, K. Iron sensitizer converts light to electrons with 92% yield. *Nat. Chem.* **2015**, *7*, 883−889.
(21) Liu, Y.; Harlang, T. C. B.; Canton, S. E.; Chábera, P.; Suarez-Alcantara, K.; Fleckhaus, A.; Vithanage, D. A.; Goransson, E.; Corani, A.; Lomoth, R.; Sundström, V.; Wärnmark, K. Towards longer-lived metal-to-ligand charge transfer states of iron(II) complexes: an *N*-heterocyclic carbene approach. *Chem. Commun.* **2013**, *49*, 6412−6414.
(22) Liu, Y.; Persson, P.; Sundström, V.; Wärnmark, K. Fe *N*-Heterocyclic Carbene Complexes as Promising Photosensitizers. *Acc. Chem. Res.* **2016**, *49*, 1477−1485.
(23) Zimmer, P.; Müller, P.; Burkhardt, L.; Schepper, R.; Neuba, A.; Steube, J.; Dietrich, F.; Flörke, U.; Mangold, S.; Gerhards, M.; Bauer, M. *N*-Heterocyclic Carbene Complexes of Iron as Photosensitizers for Light-Induced Water Reduction. *Eur. J. Inorg. Chem.* **2017**, *2017*, 1504−1509.
(24) Steube, J.; Burkhardt, L.; Päpcke, A.; Moll, J.; Zimmer, P.; Schoch, R.; Wölper, C.; Heinze, K.; Lochbrunner, S.; Bauer, M. Excited-State Kinetics of an Air-Stable Cyclometalated Iron(II) Complex. *Chem. - Eur. J.* **2019**, *25*, 11826−11830.
(25) Dixon, I. M.; Alary, F.; Boggio-Pasqua, M.; Heully. Reversing the relative ^{3}MLCT-^{3}MC order in Fe(II) complexes using cyclometallating ligands: a computational study aiming at luminescent Fe(II) complexes. J.-L. *Dalton Trans.* **2015**, *44*, 13498−13503.

(26) Braun, J. D.; Lozada, I. B.; Kolodziej, C.; Burda, C.; Newman, K. M. E.; van Lierop, J.; Davis, R. L.; Herbert, D. E. Iron(II) coordination complexes with panchromatic absorption and nanosecond charge-transfer excited state lifetimes. *Nat. Chem.* **2019**, *11*, 1144−1150.
(27) Dierks, P.; Päpcke, A.; Bokareva, O. S.; Altenburger, B.; Reuter, T.; Heinze, K.; Kühn, O.; Lochbrunner, S.; Bauer, M. Ground- and Excited-State Properties of Iron(II) Complexes Linked to Organic Chromophores. *Inorg. Chem.* **2020**, *59*, 14746−14761.
(28) Jiang, T.; Bai, Y.; Zhang, P.; Han, Q.; Mitzi, D. B.; Therien, M. J. Electronic structure and photophysics of a supermolecular iron complex having a long MLCT-state lifetime and panchromatic absorption. *Proc. Natl. Acad. Sci. U. S. A.* **2020**, *117*, 20430−20437.
(29) Chábera, P.; Liu, Y.; Prakash, O.; Thyrhaug, E.; Nahhas, A. E.; Honarfar, A.; Essen, S.; Fredin, L. A.; Harlang, T. C. B.; Kjær, K. S.; Handrup, K.; Ericson, F.; Tatsuno, H.; Morgan, K.; Schnadt, J.; Haggstrom, L.; Ericsson, T.; Sobkowiak, A.; Lidin, S.; Huang, P.; Styring, S.; Uhlig, J.; Bendix, J.; Lomoth, R.; Sundström, V.; Persson, P.; Wärnmark, K. A low-spin Fe(III) complex with 100-ps ligand-to-metal charge transfer photoluminescence. *Nature* **2017**, *543*, 695−699.
(30) Kjær, K. S.; Kaul, N.; Prakash, O.; Chábera, P.; Rosemann, N. W.; Honarfar, A.; Gordivska, O.; Fredin, L. A.; Bergquist, K.-E.; Häggström, L.; Ericsson, T.; Lindh, L.; Yartsev, A.; Styring, S.; Huang, P.; Uhlig, J.; Bendix, J.; Strand, D.; Sundström, V.; Persson, P.; Lomoth, R.; Wärnmark, K. Luminescence and reactivity of a charge-transfer excited iron complex with nanosecond lifetime. *Science* **2019**, *363*, 249−253.
(31) Pal, A. K.; Li, C.; Hanan, G. S.; Zysman-Colman, E. Blue-Emissive Cobalt(III) Complexes and Their Use in the Photocatalytic Trifluoromethylation of Polycyclic Aromatic Hydrocarbons. *Angew. Chem., Int. Ed.* **2018**, *57*, 8027−8031.
(32) Pal, A. K.; Zaccheroni, N.; Campagna, S.; Hanan, G. S. Near infra-red emission from a *mer*-Ru(II) complex: consequences of strong σ-donation from a neutral, flexible ligand with dual binding modes. *Chem. Commun.* **2014**, *50*, 6846−6849.
(33) Förster, C.; Gorelik, T. E.; Kolb, U.; Ksenofontov, V.; Heinze, K. Crystalline Non-Equilibrium Phase of a Cobalt(II) Complex with Tridentate Ligands. *Eur. J. Inorg. Chem.* **2015**, *2015*, 920−924.
(34) Förster, C.; Dorn, M.; Reuter, T.; Otto, S.; Davarci, G.; Reich, T.; Carrella, L. M.; Rentschler, E.; Heinze, K. Ddpd as Expanded Terpyridine: Dramatic Effects of Symmetry and Electronic Properties in First Row Transition Metal Complexes. *Inorganics* **2018**, *6*, 86.
(35) Otto, S.; Grabolle, M.; Förster, C.; Kreitner, C.; Resch-Genger, U.; Heinze, K. $[Cr(ddpd)_2]^{3+}$: A Molecular, Water-Soluble, Highly NIR-Emissive Ruby Analogue. *Angew. Chem., Int. Ed.* **2015**, *54*, 11572−11576.
(36) Dorn, M.; Kalmbach, J.; Boden, P.; Päpcke, A.; Gómez, S.; Förster, C.; Kuczelinis, F.; Carrella, L. M.; Büldt, L. A.; Bings, N. H.; Rentschler, E.; Lochbrunner, S.; González, L.; Gerhards, M.; Seitz, M.; Heinze, K. A Vanadium(III) Complex with Blue and NIR-II Spin-Flip Luminescence in Solution. *J. Am. Chem. Soc.* **2020**, *142*, 7947−7955.
(37) Wang, C.; Otto, S.; Dorn, M.; Kreidt, E.; Lebon, J.; Sršan, L.; Di Martino-Fumo, P.; Gerhards, M.; Resch-Genger, U.; Seitz, M.; Heinze, K. Deuterated Molecular Ruby with Record Luminescence Quantum Yield. *Angew. Chem., Int. Ed.* **2018**, *57*, 1112−1116.
(38) Fulmer, G. R.; Miller, A. J. M.; Sherden, N. H.; Gottlieb, H. E.; Nudelman, A.; Stoltz, B. M.; Bercaw, J. E.; Goldberg, K. I. NMR Chemical Shifts of Trace Impurities: Common Laboratory Solvents, Organics, and Gases in Deuterated Solvents Relevant to the Organometallic Chemist. *Organometallics* **2010**, *29*, 2176−2179.
(39) Stoll, S.; Schweiger, A. EasySpin, a comprehensive software package for spectral simulation and analysis in EPR. *J. Magn. Reson.* **2006**, *178*, 42−55.
(40) Krejčik, M.; Daněk, M.; Hartl, F. Simple construction of an infrared optically transparent thin-layer electrochemical cell: Applications to the redox reactions of ferrocene, $Mn_2(CO)_{10}$ and $Mn(CO)_3$(3,5-di-*t*-butyl-catecholate)$^-$. *J. Electroanal. Chem.* **1991**, *317*, 179−187.
(41) Schoeller, W. W.; Niemann, J. Some aspects of the electronic hypersurface of bis(methylene)phosphorane. An experimental and theoretical approach. *J. Am. Chem. Soc.* **1986**, *108*, 22−26.
(42) Rancourt, D. G.; Ping, J. Y. Voigt-based methods for arbitrary-shape static hyperfine parameter distributions in Mössbauer spectroscopy. *Nucl. Instrum. Methods Phys. Res., Sect. B* **1991**, *58*, 85−97.
(43) Lagarec, K.; Rancourt, D. G. *Recoil (1998)*, Software package v1.05 (2002); 1998.
(44) STOE & Cie *X-Area*; STOE & Cie GmbH: Darmstadt, Germany.
(45) Blessing, R. H. An empirical correction for absorption anisotropy. *Acta Crystallogr., Sect. A: Found. Crystallogr.* **1995**, *51*, 33−38.
(46) Spek, A. L. Structure validation in chemical crystallography. *Acta Crystallogr., Sect. D: Biol. Crystallogr.* **2009**, *65*, 148−155.
(47) Koziskova, J.; Hahn, F.; Richter, J.; Kožíšek, J. Comparison of different absorption corrections on the model structure of tetrakis(μ_2-acetato)-diaqua-di-copper(II). *Acta Chim. Slovaca* **2016**, *9*, 136−140.
(48) Sheldrick, G. M. SHELXT − Integrated space-group and crystal-structure determination. *Acta Crystallogr., Sect. A: Found. Adv.* **2015**, *71*, 3−8.
(49) Sheldrick, G. M. *SHELXL-2018/3*; University of Göttingen: Göttingen, Germany, 2018.
(50) Sheldrick, G. M. *SHELXL-2016/6*; University of Göttingen: Göttingen, Germany, 2016.
(51) Hübschle, C. B.; Sheldrick, G. M.; Dittrich, B. ShelXle: a Qt graphical user interface for SHELXL. *J. Appl. Crystallogr.* **2011**, *44*, 1281−1284.
(52) Neese, F. *WIREs Comput. Mol. Sci.* **2018**, *8*, e1327.
(53) Becke, A. D. Density-functional thermochemistry. III. *J. Chem. Phys.* **1993**, *98*, 5648−5652.
(54) Lee, C.; Yang, W.; Parr, R. G. Development of the Colle-Salvetti correlation-energy formula into a functional of the electron density. *Phys. Rev. B* **1988**, *37*, 785−789.
(55) Miehlich, B.; Savin, A.; Stoll, H.; Preuss, H. Results obtained with the correlation energy density functionals of becke and Lee, Yang and Parr. *Chem. Phys. Lett.* **1989**, *157*, 200−206.
(56) Neese, F.; Wennmohs, F.; Hansen, A.; Becker, U. Efficient, approximate and parallel Hartree-Fock and hybrid DFT calculations. A 'chain-of-spheres' algorithm for the Hartree-Fock exchange. *Chem. Phys.* **2009**, *356*, 98−109.
(57) Izsák, R.; Neese, F. An overlap fitted chain of spheres exchange method. *J. Chem. Phys.* **2011**, *135*, 144105−1−11.
(58) Pantazis, D. A.; Chen, X.-Y.; Landis, C. R.; Neese, F. All-Electron Scalar Relativistic Basis Sets for Third-Row Transition Metal Atoms. *J. Chem. Theory Comput.* **2008**, *4*, 908−919.
(59) Miertus, S.; Scrocco, E.; Tomasi, J. Electrostatic interaction of a solute with a continuum. A direct utilizaion of AB initio molecular potentials for the prevision of solvent effects. *Chem. Phys.* **1981**, *55*, 117−129.
(60) Barone, V.; Cossi, M. Quantum Calculation of Molecular Energies and Energy Gradients in Solution by a Conductor Solvent Model. *J. Phys. Chem. A* **1998**, *102*, 1995−2001.
(61) Schäfer, A.; Horn, H.; Ahlrichs, R. Fully optimized contracted Gaussian basis sets for atoms Li to Kr. *J. Chem. Phys.* **1992**, *97*, 2571−2577.
(62) Schäfer, A.; Huber, C.; Ahlrichs, R. Fully optimized contracted Gaussian basis sets of triple zeta valence quality for atoms Li to Kr. *J. Chem. Phys.* **1994**, *100*, 5829−5835.
(63) Grimme, S.; Antony, J.; Ehrlich, S.; Krieg, H. A consistent and accurate ab initio parametrization of density functional dispersion correction (DFT-D) for the 94 elements H-Pu. *J. Chem. Phys.* **2010**, *132*, 154104−1−19.
(64) Grimme, S.; Ehrlich, S.; Goerigk, L. Effect of the damping function in dispersion corrected density functional theory. *J. Comput. Chem.* **2011**, *32*, 1456−1465.

https://doi.org/10.1021/acs.inorgchem.1c03511
Inorg. Chem. 2022, 61, 1659−1671

(65) Plasser, F. *TheoDORE*. http://theodore-qc.sourceforge.net (accessed 2021-12-19).
(66) Plasser, F. TheoDORE: A toolbox for a detailed and automated analysis of electronic excited state computations. *J. Chem. Phys.* **2020**, *152*, 084108.
(67) Gütlich, P.; Hauser, A. W.; Spiering, H. Thermal and Optical Switching of Iron(II) Complexes. *Angew. Chem., Int. Ed. Engl.* **1994**, *33*, 2024−2054.
(68) Phan, H.; Hrudka, J. J.; Igimbayeva, D.; Lawson Daku, L. M.; Shatruk, M. A Simple Approach for Predicting the Spin State of Homoleptic Fe(II) Tris-diimine Complexes. *J. Am. Chem. Soc.* **2017**, *139*, 6437−6447.
(69) Guionneau, P.; Marchivie, M.; Bravic, G.; Létard, J.-F.; Chasseau, D. Structural Aspects of Spin Crossover. Example of the $[Fe^{II}L_n(NCS)_2]$ Complexes. In Topics in Current Chemistry; Springer: Berlin/Heidelberg, 2004; Vol. *234*, pp 97−128, DOI: 10.1007/b95414.
(70) Alemany, P.; Casanova, D.; Alvarez, S.; Dryzun, C.; Avnir, D. Continuous Symmetry Measures: A New Tool in Quantum Chemistry In Reviews in Computational Chemistry; John Wiley & Sons: Hoboken, NJ, USA, 2017; pp 289−352, DOI: 10.1002/9781119356059.ch7.
(71) De, S.; Tewary, S.; Garnier, D.; Li, Y.; Gontard, G.; Lisnard, L.; Flambard, A.; Breher, F.; Boillot, M.-L.; Rajaraman, G.; Lescouëzec, R. Solution and Solid-State Study of the Spin-Crossover $[Fe^{II}(R\text{-}bik)_3](BF_4)_2$ Complexes (R = Me, Et, Vinyl). *Eur. J. Inorg. Chem.* **2018**, *2018*, 414−428.
(72) Gütlich, P.; McGarvey, B. R.; Kläui, W. Temperature-Dependent $^5T_2(O_h) - {}^1A_1(O_h)$ Spin Equilibrium in a Six-Coordinate Cobalt(III) Complex. Investigation by ^{31}P NMR in Solution. *Inorg. Chem.* **1980**, *19*, 3704−3706.
(73) Eberspach, W.; El Murr, N.; Kläui, W. Steric and Electronic Control of Ligand Field Strength in Octahedral Co^{3+} Spin-Crossover Complexes. *Angew. Chem., Int. Ed. Engl.* **1982**, *21*, 915−916.
(74) Navon, G.; Kläui, W. Cobalt-59 NMR of a cobalt(III) spin-crossover compound. *Inorg. Chem.* **1984**, *23*, 2722−2725.
(75) Kläui, W.; Eberspach, W.; Gütlich, P. Spin-crossover cobalt(III) complexes: steric and electronic control of spin state. *Inorg. Chem.* **1987**, *26*, 3977−3982.
(76) Petzold, H.; Djomgoue, P.; Hörner, G.; Heider, S.; Lochenie, C.; Weber, B.; Rüffer, T.; Schaarschmidt, D. Spin state variability in Fe^{2+} complexes of substituted (2-(pyridin-2-yl)-1,10-phenanthroline) ligands as versatile terpyridine analogues. *Dalton Trans.* **2017**, *46*, 6218−6229.
(77) Petzold, H.; Djomgoue, P.; Hörner, G.; Lochenie, C.; Weber, B.; Rüffer, T. Bis-meridional Fe^{2+} spincrossover complexes of phenyl and pyridyl substituted 2-(pyridin-2-yl)-1,10-phenanthrolines. *Dalton Trans.* **2018**, *47*, 491−506.
(78) Evans, D. J. The determination of the paramagnetic susceptibility of substances in solution by nuclear magnetic resonance. *J. Chem. Soc.* **1959**, 2003−2005.
(79) Schubert, E. M. Utilizing the Evans method with a superconducting NMR spectrometer in the undergraduate laboratory. *J. Chem. Educ.* **1992**, *69*, 62.
(80) Piguet, C. Paramagnetic Susceptibility by NMR: The ″Solvent Correction″ Removed for Large Paramagnetic Molecules. *J. Chem. Educ.* **1997**, *74*, 815−816.
(81) Hauser, A. W. Ligand Field Theoretical Considerations. In Topics in Current Chemistry; Springer: Berlin/Heidelberg, 2004; Vol. *233*, pp 49−58, DOI: 10.1007/b13528.
(82) Connelly, N. G.; Geiger, W. E. Chemical Redox Agents for Organometallic Chemistry. *Chem. Rev.* **1996**, *96*, 877−910.
(83) Förster, C.; Heinze, K. Photophysics and photochemistry with Earth-abundant metals − fundamentals and concepts. *Chem. Soc. Rev.* **2020**, *49*, 1057−1070.
(84) Reiher, M.; Salomon, O.; Hess, B. A. Reparameterization of hybrid functionals based on energy differences of states of different multiplicity. *Theor. Chem. Acc.* **2001**, *107*, 48−55.
(85) Rudavskyi, A.; Sousa, C.; de Graaf, C.; Havenith, R. W. A.; Broer, R. Computational approach to the study of thermal spin crossover phenomena. *J. Chem. Phys.* **2014**, *140*, 184318.
(86) Bowman, D. N.; Jakubikova, E. Low-Spin versus High-Spin Ground State in Pseudo-Octahedral Iron Complexes. *Inorg. Chem.* **2012**, *51*, 6011−6019.

https://doi.org/10.1021/acs.inorgchem.1c03511
Inorg. Chem. 2022, 61, 1659−1671